

Experimental and Computational Investigations of Heat Transfer in Aero Engine Outlet Guide Vane (OGV)

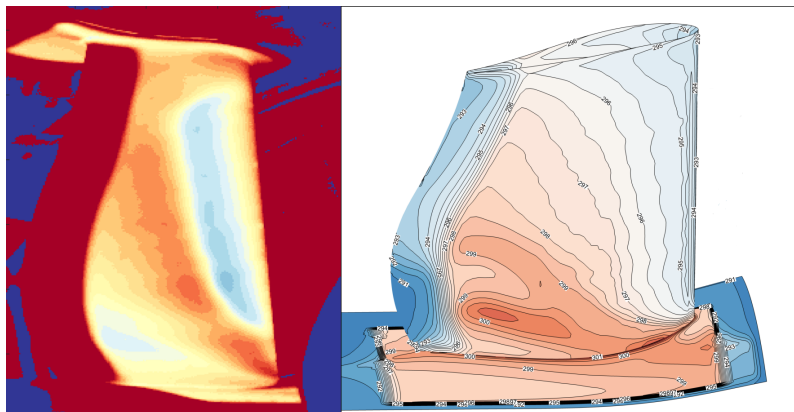
Master's thesis in Applied Mechanics Programme

RADHEESH DHANASEGARAN

MASTER'S THESIS 2018:80

**Experimental and Computational
Investigations of Heat Transfer
in Aero Engine Outlet Guide Vane (OGV)**

RADHEESH DHANASEGARAN



Department of Mechanics & Maritime Sciences
Division of Fluid Dynamics
CHALMERS UNIVERSITY OF TECHNOLOGY
Gothenburg, Sweden 2018

Experimental and Computational Investigations of Heat Transfer in Aero Engine
Outlet Guide Vanes (OGV)
RADHEESH DHANASEGARAN

© RADHEESH DHANASEGARAN, 2018.

Supervisors: Isak Jonsson and Valery Chernoray, Department of Mechanics & Maritime Sciences

Examiner: Valery Chernoray, Department of Mechanics & Maritime Sciences

Master's Thesis 2018:80
Department of Mechanics & Maritime Sciences
Division of Fluid Dynamics
Chalmers University of Technology
SE-412 96 Gothenburg
Telephone +46 31 772 1000

Cover: Measurement of Temperature using IR Thermography Experiments & CFD

Printed by Chalmers University of Technology
Gothenburg, Sweden 2018

Experimental and Computational Investigations of Heat Transfer in Aero Engine Outlet Guide Vanes (OGV)

RADHEESH DHANASEGARAN

Department of Mechanics & Maritime Sciences
Chalmers University of Technology

Abstract

In modern aircraft gas turbine engines, the turbine rear structure (TRS) located downstream of the low-pressure turbine (LPT), plays a significant role in de-swirling the flow from the LPT and currently considered as a potential LPT noise reduction device. The TRS is composed of the outlet guide vanes (OGVs) which establish a structural support between the aft bearing support and the main engine case. In future aero-engine designs, the flow that exits from the LPT will have greater amounts of swirl, which imposes a new demand on the TRS aero-design. Furthermore, as the engine conditions are subjected to change, during the take-off and landing, apart from its regular operations, the swirl angle at the inlet of OGV will be very large, leading to even large operating range. While operating at these off-design conditions, the vanes are subjected to the high amount of aerodynamic and thermal loads. Therefore, the heat transfer characteristics need to be studied in detail for an efficient design of these components.

In the present study, an experimental and computational investigation of heat transfer is carried out on an OGV. The experiments are carried out at the Chalmers Turbine Test facility which is an annular cascade tunnel with an upstream LPT 1.5 stage. The heat transfer measurement is performed on the vane and hub sector. The heated model is prepared by the rapid prototyping and allows a uniform heat supply to the highly three-dimensional surface of the OGV and hub. Infrared (IR) Thermography is used to measure the vane and hub surface temperature leading to the estimation of the heat transfer distribution. The IR camera and reference thermal sensors are well calibrated before the experiments. A commercial CFD solver is used to solve the governing flow and heat transfer equations with the SST $k-\omega$ and Standard $k-\epsilon$ turbulence models for adiabatic solving and SST $k-\omega$ model for Conjugate solution. The results from the computational studies are validated with the experimental data. The major aim of this study is to establish an accurate technique for measurements of the heat transfer distribution on OGVs.

Keywords: OGV, Heat Transfer, Infrared Thermography, Experiments, CFD

Acknowledgements

Words are infinitesimal to express my gratefulness to my supervisors Isak Jonsson & Prof. Valery Chernoray for the endless guidance throughout this one academic year Master Thesis. The profound knowledge they had in the fascinating area of experiments always inspires a novice like me to reach those heights. I must be thankful to Prof. Valery Chernoray once again for giving me this wonderful opportunity to venture into the area of experimental heat transfer, which I was longing these years. Isak Jonsson, the man behind the screens, who directed me to carry out this research and he is the one of the best all-rounders I have seen, and keeps me motivated.

I wish to thank my dear brother Shankaranand for helping with the initial design phase which had a strong basement for this work. I must be thankful to my friends Ssheshan & Aravind in India for their selfless support in formulating the computational meshing process, in spite of my pester during their valuable time. I extend it to Bercelay, Wenbo & Guglielmo at the Fluid Dynamics division and Srikanth at the GKN Aerospace Sweden AB for their valuable time and suggestions regarding the CFD mesh generation again. Also, I would like to thank Dr. Loli Paz at the Chemistry department for providing the Ultrasound measurement device at the necessary times. I would like to thank Anirudh for his kind support during the earlier project course work that gave me a gateway to experimental research where I happened to meet Isak & Prof. Valery. Alessandro, my best ever buddy in the lab who made me more social even outside the work arena, so words are again not enough to thank him. Apart from the work, there were a lots of wonderful 'fika' discussions with the people at the division which I will never get back. I extend it to Sherif, though it would be a short time interaction, it was a great support.

I further extend my gratitude to Prof. Lars Davidson for illuminating my knowledge in the area of Fluid dynamics during the coursework and he is one of the best teachers that I have ever seen. Having been in the Fluid dynamics division at Chalmers, was a beautiful journey with lots of new learning experiences everyday throughout this one magnificent year and it is hard for me to realize that it has come to an end. Overall the Masters life in Sweden is the most important phase of my life, with extremity of emotions that transformed myself from a conservative towards a rational thinking and it was a wonderful journey.

And I would like to thank my mentors Dr. Rajesh Kumar Panda & Prof. LakshmiNarasimhan in India, who always have an important role in shaping my career. Also I extend it to Prof. B.V.S.S.S.Prasad at the IIT Madras, for his valuable guidance during my tenure over there. All their supports and encouragements made my Masters dream possible.

Also, I further extend my thanks to all the friends during and outside this Masters life for their wonderful time and support. Especially Nagacharan for his kind company during the cooking time and serving as a strong mental support during my difficult times. I extend my thanks to the friends and people at IIT Madras.

Finally but not the last, all these things wouldn't be possible without the endless supports and sacrifices by my beloved parents right from my childhood which for sure cannot be replaced with anything. My dear girlfriend Chithra, I thank her for bearing with me in spite of this long-distance, time and all my frustrations, she has been a strong support and motivator. They have been an integral part in making my dreams true all these years with their sacrifices. I am grateful to them and my dear sister and brother. Therefore I dedicate this to them.

Radheesh Dhanasegaran, Gothenburg, June 2018

**Dedicated
To
My Dear Parents, My Better-half,
Dr.B.R.Ambedkar & Periyar**



Contents

List of Figures	xv
List of Tables	xvii
1 Introduction	1
1.1 Outlet Guide Vane Heat Transfer	1
1.2 Measurement Techniques	2
2 Review of literature	3
2.1 Studies on Turbine Flow & Heat Transfer	3
2.2 Studies on OGV Heat Transfer	4
2.3 Studies on Infrared Camera Non-Uniformity Correction(NUC) and Calibration	4
2.4 Studies on IR Thermography Measurement Quantification	4
2.5 Studies on Mesh Refinement studies	5
3 Theory & Design Methodology	7
3.1 Background	7
3.2 Heat Transfer Mechanism	7
3.2.1 Heat Transfer by Conduction	7
3.2.2 Heat Transfer by Convection	7
3.3 Design of the Vane Heating System	8
3.3.1 First CAD Model	8
3.3.1.1 CFD Test	9
3.3.1.2 Structural Test	10
3.3.2 Second CAD Design	10
3.3.2.1 CFD Test	11
3.3.2.2 Structural Test	12
3.3.3 Outcomes of the Preliminary Design	13
3.3.4 Final CAD Model	13
3.3.4.1 Design of the Vane Channel	13
3.3.4.2 Design of the Hub Channel	16
3.3.4.3 Design of the Shroud Channel	17
3.3.4.4 Assembly	18
4 Experimental Methodology	21
4.1 Experimentation	21

4.1.1	Rapid Prototyping of the OGV	21
4.1.2	IR Camera System Calibration	22
4.1.2.1	Background	22
4.1.2.2	IR Camera	22
4.1.2.3	Calibrator	22
4.1.2.4	Bad Pixel Association & NUC	24
4.1.2.5	Calibration Process	26
4.1.3	Hot water circulation system	27
4.1.4	Preliminary Wind Tunnel test	30
4.1.5	The Experimental Test Rig	31
4.1.5.1	Driving Fan	31
4.1.5.2	Diffusing section	32
4.1.5.3	Heat Exchanger section	32
4.1.5.4	Settling Chamber	32
4.1.5.5	Contraction section	32
4.1.5.6	Turbine section	32
4.1.5.7	TRS section	33
4.1.6	Uncertainty Quantification	33
4.1.6.1	Uncertainty in k	33
4.1.6.2	Uncertainty in t	33
4.1.6.3	Uncertainty in T_{H_2O}	33
4.1.6.4	Uncertainty in T_{wall}	33
4.1.6.5	Uncertainty in ε_r	34
5	Computational Methodology	35
5.1	Pre-processing	35
5.1.1	Physical Configurations & Grid Generation	35
5.1.2	Boundary conditions	38
5.2	Grid Convergence study	39
5.3	Solving Methodology	40
5.3.1	Governing Equations	40
5.3.1.1	Continuity equation	41
5.3.1.2	Momentum equation	41
5.3.1.3	Energy equation	41
5.3.2	Turbulence Model	41
5.3.3	Spatial Discretization Schemes	41
5.4	Data Representation	42
6	Results & Discussions	43
6.1	Post Processing of the Experimental Results & Estimation of Heat Transfer Coefficient	43
6.2	A Brief Review of Secondary Flow Influence on Heat Transfer	44
6.3	Temperature Distribution	44
6.4	Heat Transfer Coefficient Distribution	48
7	Conclusion	51
7.1	Scope for Future Work	52

References

53

List of Figures

1.1	TRs in the Aero Engine Gas Turbine	1
3.1	First Design	8
3.2	First Design FV Mesh	9
3.3	First Design Total Pressure	9
3.4	Structural BC	10
3.5	Design1 Deformation	10
3.6	Second Design	11
3.7	Second Design FV Mesh	11
3.8	Second Design Total Pressure	12
3.9	Second Design Deformation	12
3.10	Second Design Deformation for AWA Total Pressure	13
3.11	Vane Split	14
3.12	Vane offset	14
3.13	Pinned support	15
3.14	Vane solid model	15
3.15	Vane	16
3.16	Vane TE	16
3.17	Hub cut section view	17
3.18	Hub model	17
3.19	Shroud cut section view	18
3.20	Shroud	18
3.21	Assembled model cut section view	19
3.22	Assembly	19
4.1	OGV Coated with NVC	21
4.2	Calibration System Design	24
4.3	Frame with Bad Pixels	25
4.4	Raw image with NUC applied	26
4.5	Calibration of wide angled lens	27
4.6	Calibration of narrow angled lens	27
4.7	Circulation System Schematic	28
4.8	OGV with Hot water circulation	29
4.9	Improved CAD Model	29
4.10	Additional Support Structures	30
4.11	Preliminary Wind Tunnel Test	31
4.12	Chalmers EEC Test Rig Schematic	31

5.1	Adiabatic Case Domain	36
5.2	Conjugate Case Domain	36
5.3	Adiabatic Case Mesh	37
5.4	Conjugate Case Mesh	37
5.5	Zoomed view of the OGV and End-walls.	38
5.6	Grid Convergence study	40
5.7	Mid-span Plane	42
5.8	Mid-span curve	42
6.1	Contours of Temperature Distribution	45
6.2	$\phi = 0.622$ -Comparison of Mid-span Temperature Distribution	46
6.3	$\phi = 0.657$ -Comparison of Mid-span Temperature Distribution	46
6.4	$\phi = 0.588$ -Comparison of Mid-span Temperature Distribution	47
6.5	Overall Comparison of Experimental & Conjugate CFD Temperature Distribution	47
6.6	Overall Comparison of Experimental & Conjugate CFD HTC Distri- bution	48
6.7	Contours of HTC Distribution	49

List of Tables

4.1	Accura Clearvue material properties	22
4.2	MWIR Phoenix Camera System Specifications	23
4.3	Wind Tunnel Specifications	32
5.1	Details of the boundary conditions	39
5.2	Details of the Grid Convergence study	40
6.1	Test matrix	43

1

Introduction

1.1 Outlet Guide Vane Heat Transfer

The present day aircraft gas turbines have increased operating temperatures resulting from the high overall pressure ratio giving a wider operating range for the low pressure turbine (LPT), the outlet guide vanes (OGVs) play a significant role to maintain the flow in the axial direction. In general, the flow that exits from the LPT will have a greater amount of swirl. These OGVs also establish a structural support between the aft bearing support and the main engine case. The design of OGV is similar to the turbine blade or vane in terms of geometry and the flow field. The engine with the TRS is shown in the figure below. As the engine conditions are subjected to change, during the take-off and landing, apart from its regular operations, the swirl angle at the inlet of OGV will be very large, leading to operating in both on and off-design conditions. While operating at these off-design conditions, the vanes are subjected to the high amount of aerodynamic and thermal loads.

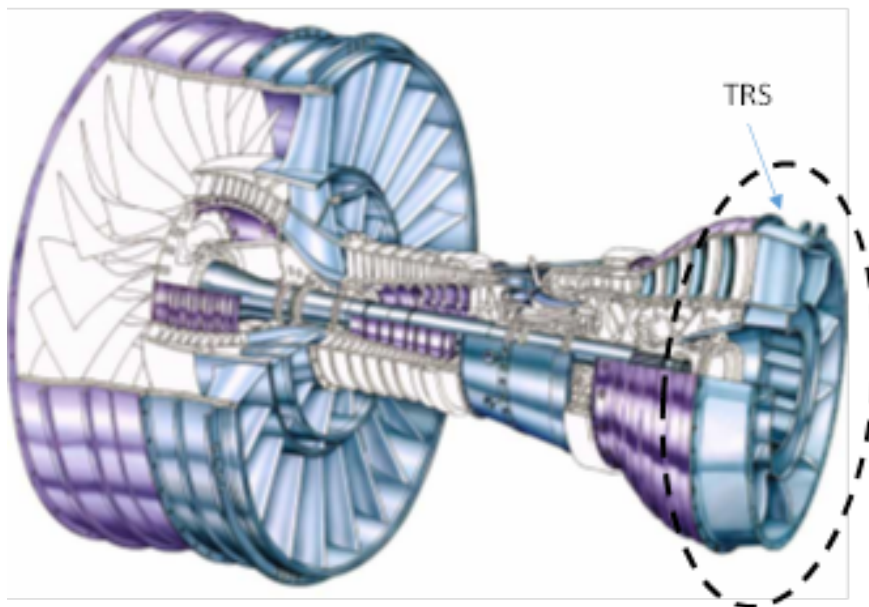


Figure 1.1: TRS in the Aero Engine Gas Turbine

In the future second generation of geared engines, a higher overall pressure ratio will result in increased operating temperatures. The future engines will also have higher by-pass ratios, i.e., larger fan with relatively smaller engine cores, which therefore

has a wider operating envelope for the LPT. Furthermore, the components in these engines will need to be lighter and for the components in the gas path, they will need to have lower pressure losses. For the OGV, this development implies that designs are needed that: can withstand higher temperatures and temperature variations, can operate under more severe LPT off-design conditions, present lower pressure losses, and that are lighter. Therefore, the heat transfer characteristics need to be studied in detail for an efficient design of these components..

1.2 Measurement Techniques

Measurement of the heat transfer distribution on the OGV, being the prime objective of this study, involves challenges with accuracy and the choice of suitable technique. With the conventional measurement devices like thermocouples to some advanced techniques like the LCT, IR Thermography, each technique has its own advantages and limitations. Therefore, choosing an optimum technique with respect to the conditions involved is an important part of the experimental studies. The advantages and limitations are observed in the following section.

The Thermocouples (TC), in general can be applied to measure temperature on any flat conductive element. It has the hot and cold junctions, with separated leads made of different materials. There are different types of TCs viz. J, K, T, E, R, S and B used based on the application type. They have advantages like low cost, wide temperature operating range, high resolution and durability. However, they suffer from short comings like need for signal amplification, poor sensitivity & stability, non-linearity and tedious calibration process. The Resistance Temperature Detectors (RTDs), however offers better reliability, accuracy, stability and re-calibration compared to the TCs, still suffers from high cost, slow response, limited temperature of 1000 K and sensitivity. Also, these two methods function good only for single point temperature measurements. But to get an effective temperature distribution over multiple points, advanced methods need to be employed.

One such method is the Liquid Crystal Thermography (LCT), which uses Thermochromic Liquid Crystal (TLC) for surface temperature measurements. These TLCs changes color as a function of temperature when illuminated by visible white light. Therefore, the relationship between the temperature and color response (calibration) should be understood properly to measure with TLC. This method offers high spatial resolution, cost effectiveness, simpler calibration and high accuracy. But it is limited to uncertainties with high lightning angles, poor reflection at lower coating thickness, stable white light requirement, in-situ calibration & experimentation. Also, the measuring environment should be free from IR and UV radiations.

The infrared Thermography is one of the most successful techniques, with the object itself being the source for radiation. Also, temperature measurements on a moving object is possible with this technique. It is non-intrusive, excellent for surface temperature measurements. But there are also a few shortcomings which challenges this technique like shading, dark spot formation (narcissus effect) and poor accuracy with varying emissivity. In the present study, an experimental heat transfer measurements on an aero-engine OGV has been carried out using IR Thermography technique with supporting computational studies.

2

Review of literature

2.1 Studies on Turbine Flow & Heat Transfer

Local variation of the heat transfer coefficient around gas turbine blade nozzle guide vane cooling has been experimentally investigated by Turner[1]. A numerical differentiation scheme for obtaining the temperature gradient on the outer wall has been used that could be directly related to the local heat transfer coefficient.

Endwall and Airfoil surface heat transfer distributions have been experimentally studied by Graziani et al.[2] for a linear cascade turbine blade model using Chromel-Alumel thermocouples. The significance of passage secondary flow influence on the endwall and suction surface heat transfer are greatly illustrated.

The effects of secondary flow vortex structures on endwall boundary layer characteristics through turbine blade passages have been experimentally investigated by Sieverding[3].

Heat transfer investigations using IR thermography experiments and CFD simulations for an aggressive intermediate turbine duct(ITD) in [7] & [8] and comparisons are made between them that had reasonable agreements. The incoming flow features and the tip leakage flow had significant effect on the heat transfer performance on endwalls and duct in the experiments. The corresponding CFD studies also showed the same results with little variations.

A transient liquid crystal measurements for a turbine blade leading edge impingement cooling with normal and tangential jets has been conducted by Wang et al.[20]. The transient process was initiated by a sudden introduction of heated air to the test section. A CCD camera was used for optical measurements from the TLC with the image being recorded for every 0.5 seconds and for viewing angles 90° and 45° . The liquid crystals are calibrated in-situ with the help of nine thermocouples but without the jet flow . The overall uncertainty in heat transfer calculations was found to be 5%.

Criss-Cross patterned rib turbulators across a square duct, with inline and staggered fashion have been studied by Singh et al.[16] with the aim of developing higher thermal-hydraulic performance. Transient liquid crystal thermography has been handled for heat transfer measurements. The mainstream temperature was

varied from room temperature to low temperatures over the time for the transient experiments. A hue-based calibration technique was followed with the aid of two T-type thermocouples for the Thermochromic Liquid Crystals. The uncertainty in the Nusselt number was found to be less than 12%.

2.2 Studies on OGV Heat Transfer

Experimental heat transfer investigations on an outlet guide vane in a linear cascade model Liquid Crystal Thermography(LCT) by Wang et al.[11]. Their conclusions are there is a significant effect of incidence angle on the endwall heat transfer.

An experimental heat transfer measurement technique in linear cascade of an OGV and endwall has been investigated by Merina[12] to evaluate the heat transfer coefficient. The results showed higher heat transfer coefficient values corresponding to the interaction area between the OGV and endwall.

Heat transfer studies using experimental and numerical investigations of OGV and endwall with various inlet flow angles has been carried out again by Wang[13]. LCT technique for experiments and three different RANS based turbulence models have been used. The effects of the horse-shoe vortex seemed to be predominant on the heat transfer near the OGV leading edge and the passage between the OGVs. However all the three RANS based models captured the main features of the heat transfer in the pressure side, a significant over-prediction was seen in the suction side at both on and off-design conditions.

2.3 Studies on Infrared Camera Non-Uniformity Correction(NUC) and Calibration

A comparison of advanced calibration methods for IR camera and the NUC procedure has been presented by Marcotte et al.[9] and assessed their advantages and limitations.

A Non-Uniformity Correction for IR focal-plane array with efficient pixel offset estimation based on linear correction scheme has been proposed by Orzanowski[15], that permitted to remove optics shading effect.

2.4 Studies on IR Thermography Measurement Quantification

Aerothermal investigations of the flow and heat transfer in a helically corrugated channel were conducted by Mayo et al.[14]. An inconel foil is used for heating the internal corrugated cylindrical surface. Liquid Crystal Thermography was used for measuring the inner wall temperature, whereas Infrared Thermography is used for

external surface measurements. A Matt black paint layer was coated upon the TLC layer for enhanced contrast, followed by an acrylic adhesive and an Inconel foil. The overall uncertainty on the temperature measurements was found to be less than $\pm 0.75^\circ C$.

An engine-realistic NGV endwall cooling configuration was studied experimentally and computationally by Ornano & Povay[17] using Infrared Thermography technique. The endwalls and combustor simulator were manufactured from Rohacell, a low thermal conductivity material ($k=0.003 \text{ Wm}^{-1}\text{K}^{-1}$) for IR measurements. Two FLIR (A655sc) IR cameras were used and the endwalls were coated with high emissivity ($\varepsilon=0.97$) Autotek black paint. An in-situ calibration is made for the IR cameras with both the mainstream and coolant flows being turned on.

A novel approach for evaluating heat transfer in the advanced rotor blades has been proposed by Elfner et al.[18]. A high resolution Infrared Thermography technique has been employed that enables measurements on strongly cooled and strongly curved surfaces. A FLIR SC600 IR camera was used with three optical access provisions with a cooled InSb detector and a high emissivity Nextel Velvet Coating (NVC) for the curved surface. An extensive pre-calibration and final in-situ calibration has been performed for radiation correction. The compressed air exchanging heat with a natural gas fired heat exchanger was used to supply hot air whereas the cold air being supplied from the same compressor bypassed to another heat exchanger.

2.5 Studies on Mesh Refinement studies

A uniform reporting of grid refinement studies using Grid Convergence Index (GCI) in CFD has been proposed by Roache[4] based upon a grid refinement error estimator derived from Richardson Extrapolation.

2. Review of literature

3

Theory & Design Methodology

3.1 Background

In this section, the theory behind the heat transfer mechanism governing the present study and the design methodology involved in creating the OGV model for the heat transfer experiments is discussed in detail.

3.2 Heat Transfer Mechanism

In general, all the real-time heat transfer problems involves transfer by all the three basic modes of heat transfer such as conduction, convection and radiation. But the most dominant and important phenomena among them are the conduction and convection.

3.2.1 Heat Transfer by Conduction

The energy transfer that occurs due to the prevailing temperature difference in a body especially a solid, from a higher to lower temperature region. The heat transfer per unit area is proportional to the normal temperature gradient.

$$q_x = -kA \frac{\partial T}{\partial x} \quad (3.1)$$

where

q_x - heat-transfer rate

$\frac{\partial T}{\partial x}$ - temperature gradient in the heat flow direction

k - thermal conductivity of the material

3.2.2 Heat Transfer by Convection

The heat transfer phenomena that occurs between the fluid and solid surface in case of a flow over a solid body or flow inside a channel due to the existence of the temperature difference between the fluid and solid wall, is termed as convection. This fluid motion can be either artificially induced or naturally occurring, where the former process is called forced convection and the latter is called free or natural convection. By Newton's law of cooling,

$$q = h(T_w - T_f) \quad (3.2)$$

where

q - heat flux from hot wall to cold fluid

h - convective heat transfer coefficient

T_w - Wall Temperature

T_f - Fluid Temperature

Equation (3.2) can also be written alternatively as $q = h(T_f - T_w)$ which implies heat transfer from hot fluid to the cold wall.

3.3 Design of the Vane Heating System

In this section, the procedure followed during the CAD modelling of the heating channel design is explained in detail. A surface modelling approach has been followed and later the solid model is constructed out of it. Initially the design was made out of a single component blade assembly. But, due to constraints in the feature extractions, this method is dropped and a vane surface dependent design is followed for simplified and an elegant approach. This will very advantageous in adapting to future vane profile modifications. The vane, hub and shroud are created as individual part geometries and finally assembled together as a single component. The procedure is explained in chronology in the following sections.

The heating channel designs have been tested for its robustness with respect to flow and structural tests. Before 3D printing, the designed CAD model has to qualify these two tests.

3.3.1 First CAD Model

In this design, a constant outer wall thickness of 4 mm and channel height of 3 mm have been implemented. The water after heating the blade walls, is allowed to exit in the two directions near the leading and trailing edges and flow through the outlet pipe. The CAD model for design 1 is shown in the figure 3.1.

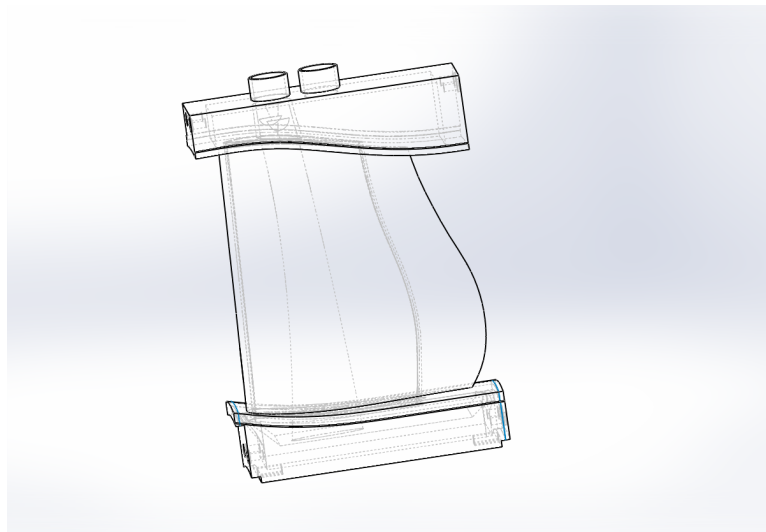


Figure 3.1: First Design

3.3.1.1 CFD Test

The model is then cleaned up for performing flow analysis. All the unwanted surfaces are removed and the mesh is generated for the flow path using finite volume mesh generating tool ICEM CFD from ANSYS. A relatively fine tetrahedron elements is used for generating the background grid and the final grid size contained about 0.5 million cells shown in figure 3.2. The flow is able to turn through the designed channel and exits through the outlet. And finally the total pressure has been evaluated. It is seen that the maximum total pressure occurs on the blade tip near the inlet region which is found to be 0.0135 MPa. The area weighted average value of total pressure on the entire blade surface is found to be 0.01145 MPa shown in figure 3.3.

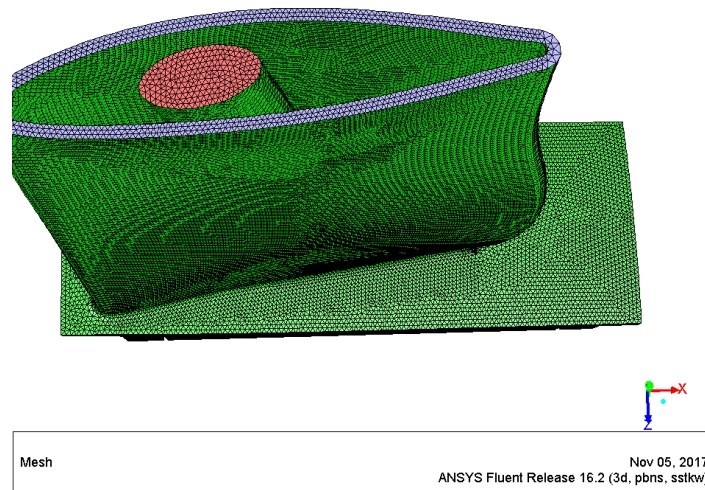


Figure 3.2: First Design FV Mesh

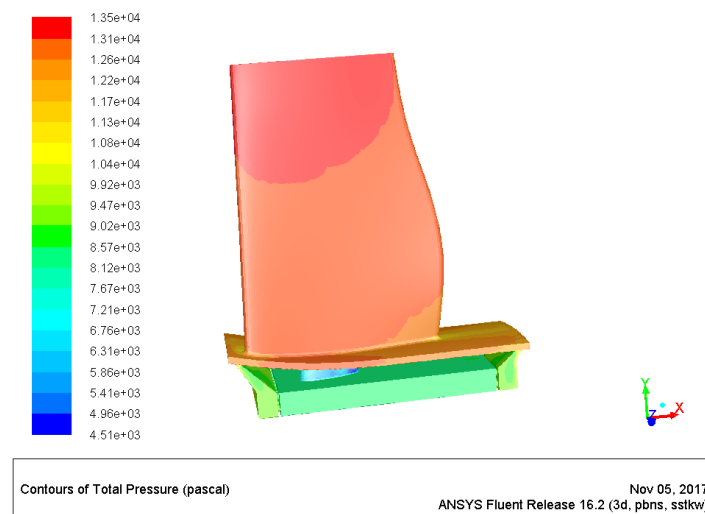


Figure 3.3: First Design Total Pressure

3.3.1.2 Structural Test

The total pressure value is fed as the input value for the structural analysis. This analysis is performed using ANSYS Static Structural tool. The structural domain is extracted from the CAD model shown in figure 3.4. The pressure boundary is applied on the inner wall and the ends are fixed. The total deformation is maximum at the centre of the pressure surface. Its value is found to be 2.09 mm which is quite maximum that can be seen from figure 3.5.

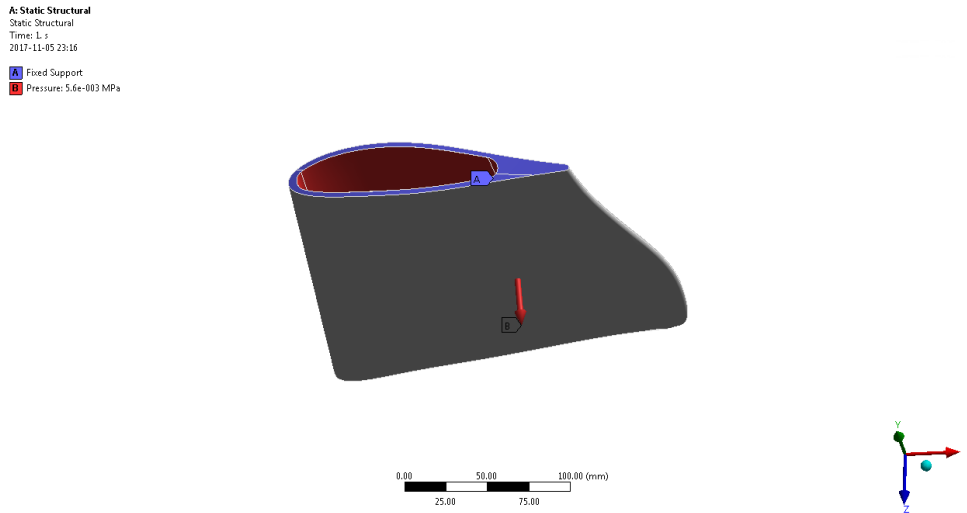


Figure 3.4: Structural BC

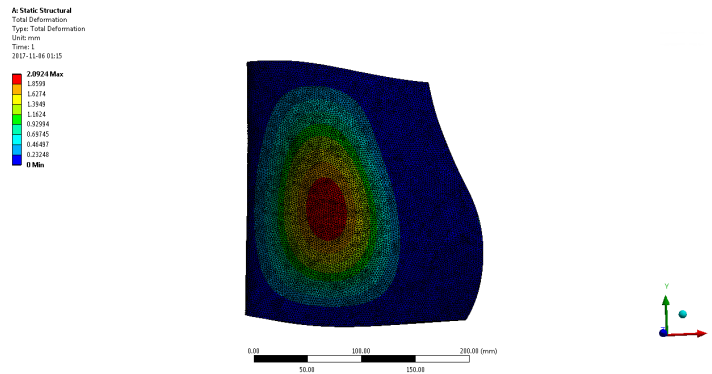


Figure 3.5: Design1 Deformation

3.3.2 Second CAD Design

In this design, the same outer wall thickness and channel as in first design have been maintained. The water after heating the blade walls, is allowed to exit in all the four

directions and the outlet pipe area is maximized to reduce the pressure losses. The CAD model for design 2 is shown in the figure 3.6.

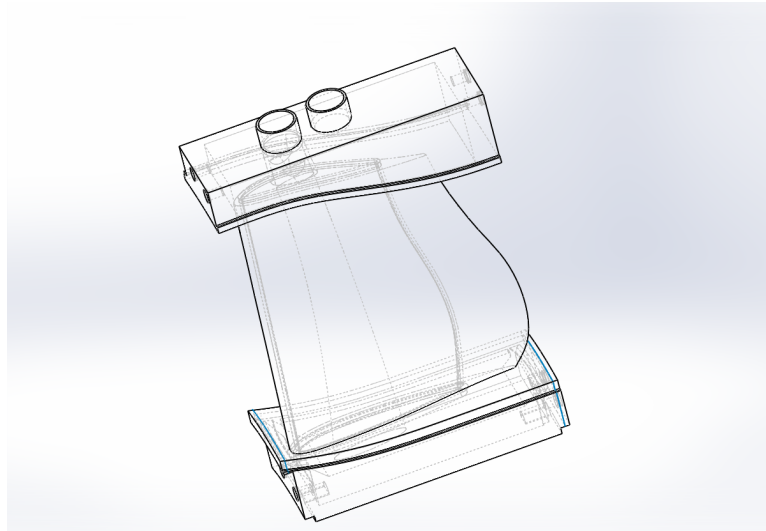


Figure 3.6: Second Design

3.3.2.1 CFD Test

A very fine tetrahedron elements is used for generating the background grid and the final grid size contained about 4 million cells shown in figure 3.7. The flow is able to turn through the designed channel and exits through the outlet with reduced losses compared to design 1. And finally the total pressure has been evaluated. It is seen that the maximum total pressure occurs on the blade tip near the inlet region which is found to be 0.0054 MPa. The area weighted average value of total pressure on the entire blade surface is found to be 0.0037 MPa shown in figure 3.8.

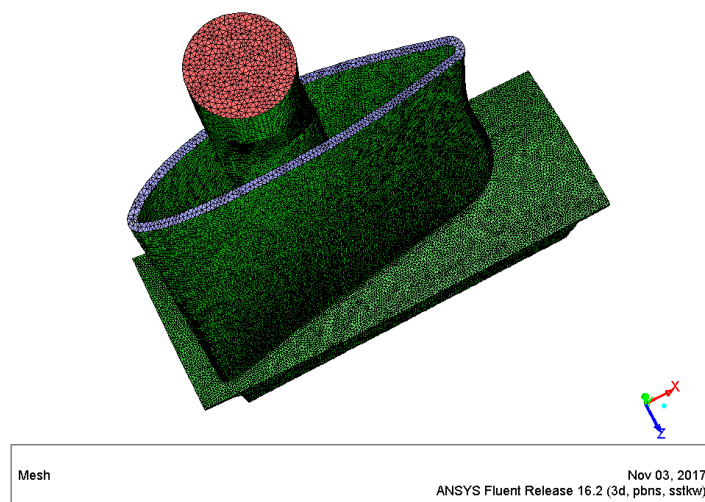


Figure 3.7: Second Design FV Mesh

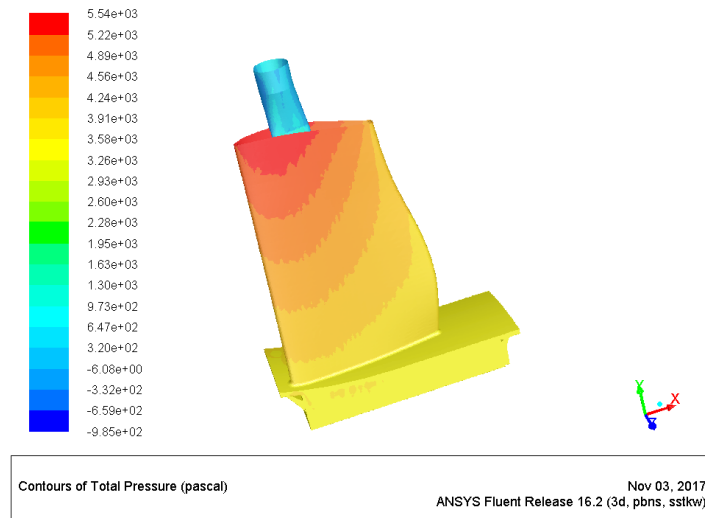


Figure 3.8: Second Design Total Pressure

3.3.2.2 Structural Test

The same procedure is followed for the structural analysis as in design 1. The total deformation is again maximum at the centre of the pressure surface. Its value is found to be 0.85 mm for the maximum pressure load but for the averaged load it is further reduced to 0.58 mm.

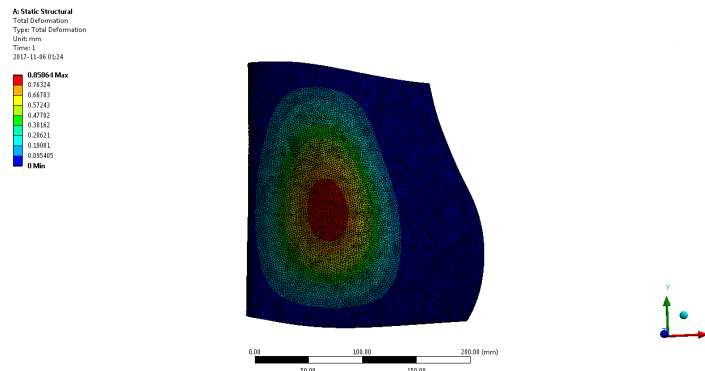


Figure 3.9: Second Design Deformation

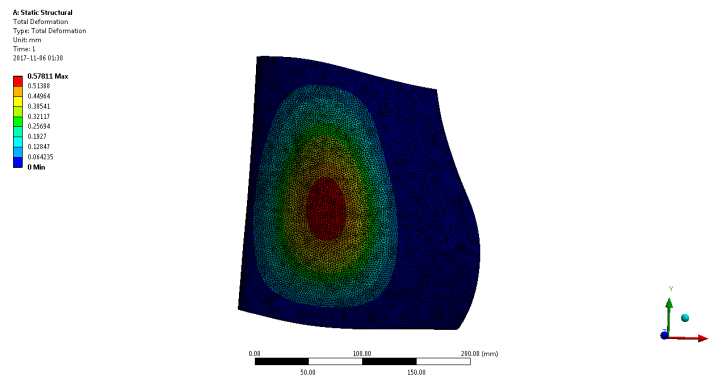


Figure 3.10: Second Design Deformation for AWA Total Pressure

3.3.3 Outcomes of the Preliminary Design

It is seen that the first design though passing the CFD test, failed the structural test. Therefore, a second improvised design has been made and tested correspondingly. The deformation has been greatly reduced in the second model, which can be taken for fabricating the physical model of the OGV.

3.3.4 Final CAD Model

3.3.4.1 Design of the Vane Channel

The lofted surface of the vane is used as the reference geometry for all the part construction. To create a thickness for the vane wall and a channel inside the vane, the outer vane wall has to be offset internally. But this feature seemed to be impossible with the current geometry, as its highly 3D and the offset resulted in curve intersection near the trailing edge. To avoid this, the vane is split at a distance of 30 mm approximately from the trailing edge shown in figure 3.11. The first offset to create a wall thickness is thus made 4 mm internally. A uniform thickness is generated for the outer wall to enable uniform conduction. This surface is again offset to 3 mm for creating the channel. The vane is cut 4 mm external offset from the hub line and 2 mm external offset from the shroud line to make provisions during the assembly and trim away the unwanted features shown in figure 3.12. Then the inner core is made solid by using 'Surface Fill' feature. To hold this inner core, two cylindrical pinned supports of 1 mm diameter each are created from the channel outer wall in the pressure and suction surfaces by extrusion features shown in figure 3.13. Finally, a series of markers of 1 mm diameter radius and depth are made either side on the pressure and suction surfaces shown in figure 3.14 & figure 3.15, to make them visible distinct in the IR camera measurements. These markings are made by extracting curves on the vane surface in the span-wise direction and series of creating cylinders using 'Curve driven Pattern' feature finally subtracting them

from the vane. These holes will be filled with material like silver paint making their appearance distinct in the IR camera. The split portion of the trailing edge shown in figure 3.16, is modelled as a separate part in a similar manner and will be joined during the assembly process. With this design, a maximum uniform surface heating is possible covering more than 80% of the OGV span.

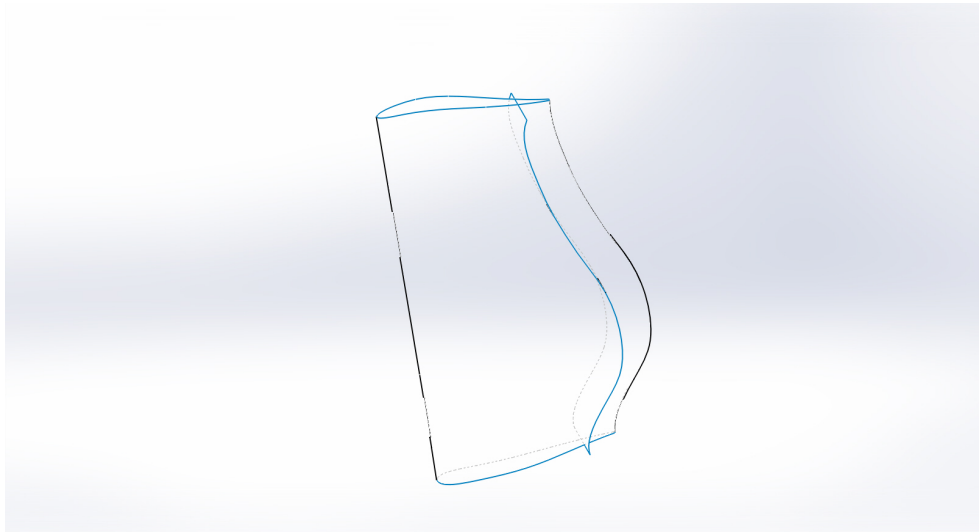


Figure 3.11: Vane Split

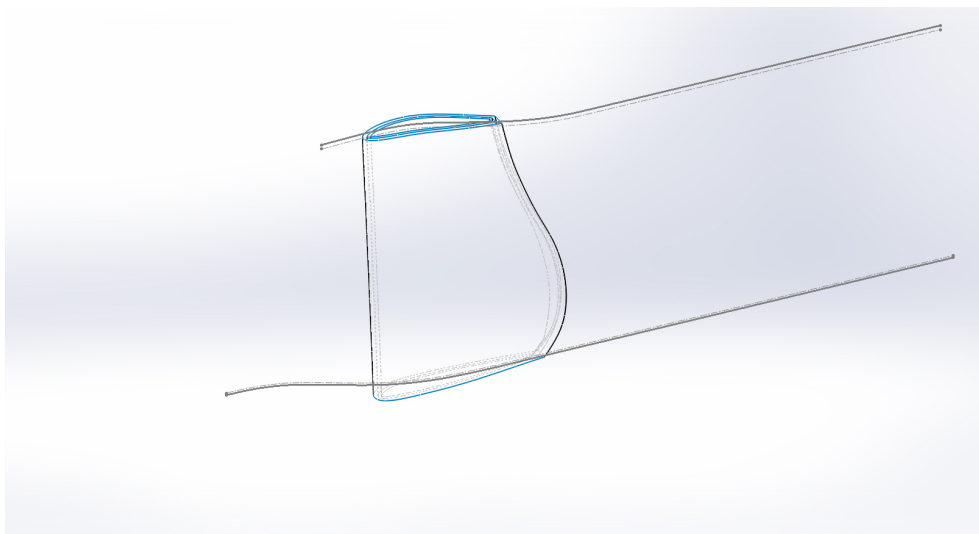


Figure 3.12: Vane offset

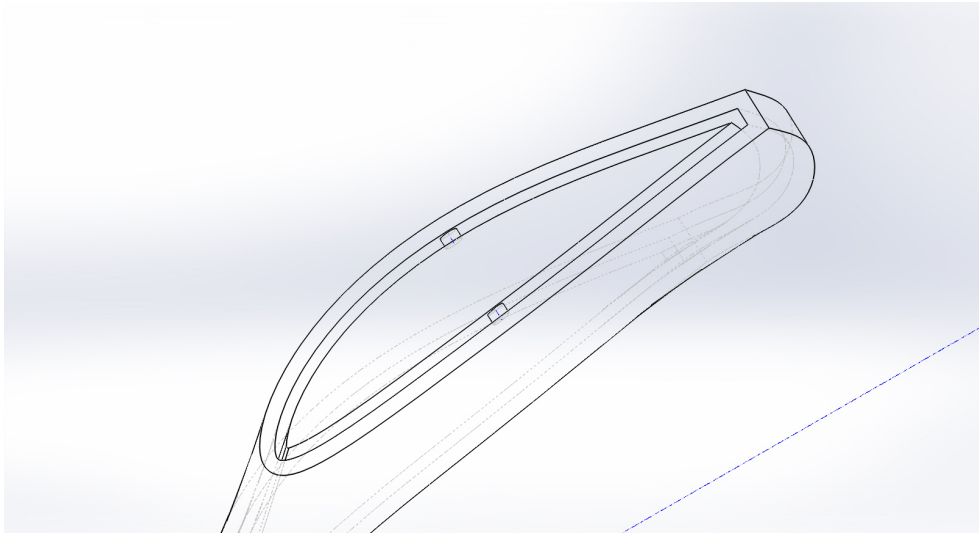


Figure 3.13: Pinned support

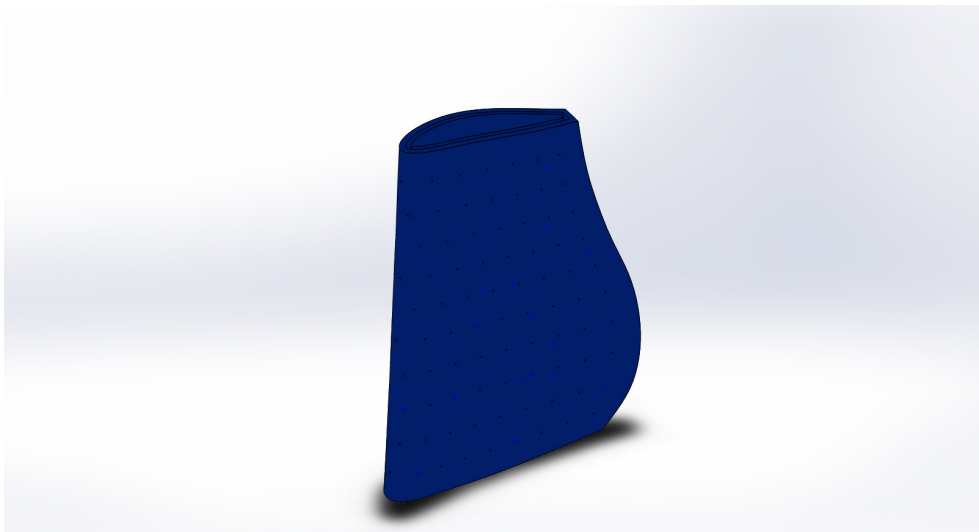


Figure 3.14: Vane solid model

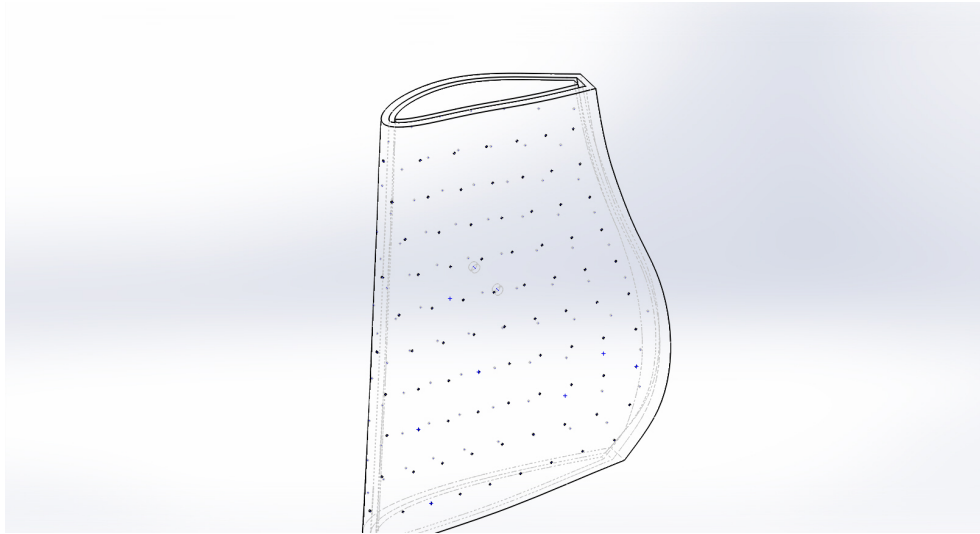


Figure 3.15: Vane

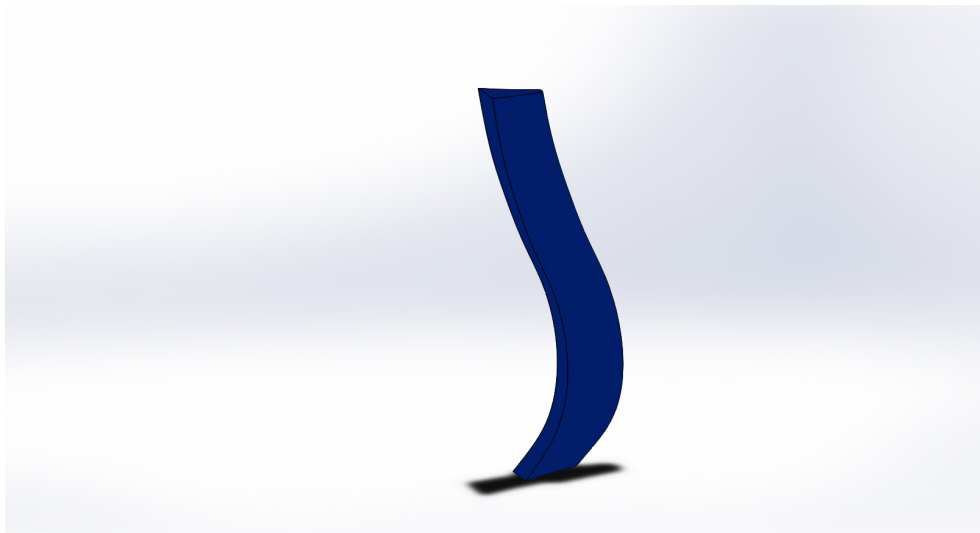


Figure 3.16: Vane TE

3.3.4.2 Design of the Hub Channel

The hub design is the next challenging part, as it contains sharp corners, the return channel entry and seating for the central core. The hub is extended along the suction surface up to the hub of the next vane by using revolve feature. This extension will provide additional heat transfer data on the hub endwall where the interesting features are sought to occur. The revolved solid is split with the vane outer wall to pave the opening for the water channel and the inner core is retained. This inner core is again trimmed from a distance of 7.10 mm below the hub line, to make the vane possibly seated inside the hub. Then, the internal channel is made such that it enables maximum heating of the hub endwall and revolved. Four square pillars have been created that could hold the hub seating for the vane inside the channel. The leading and trailing faces of the outer walls are grooved 0.2 mm inside, to avoid

metal contact thus restricting heat conduction losses through these faces. Markers are created on the hub surface in a similar way to the vane markers. Chamfers on the sides are created based on the details from the drawing.

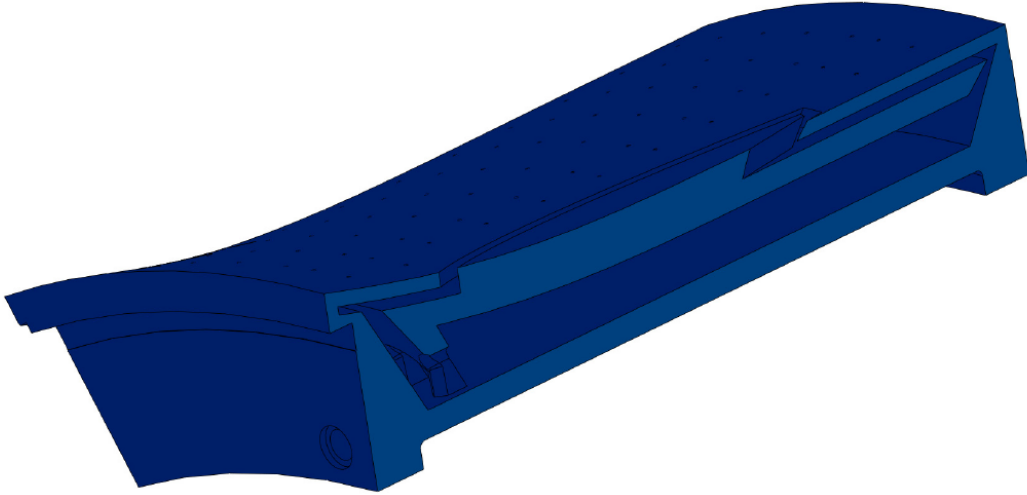


Figure 3.17: Hub cut section view

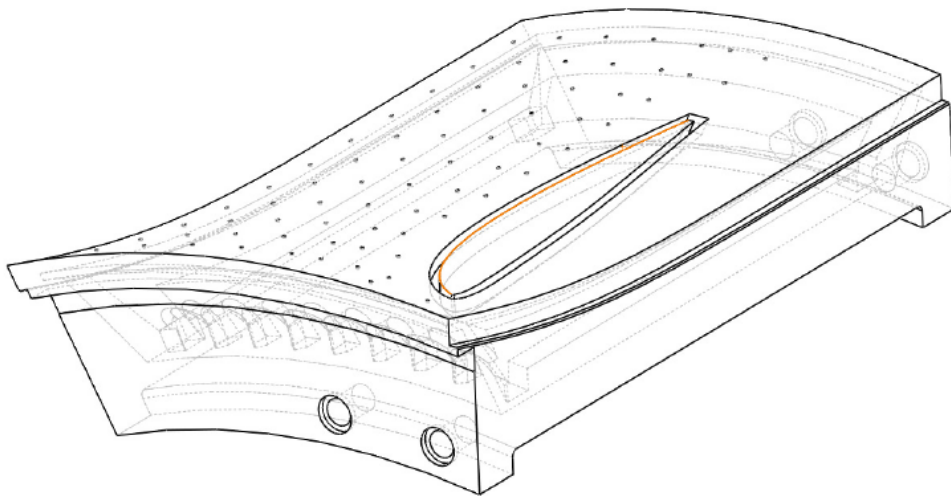


Figure 3.18: Hub model

3.3.4.3 Design of the Shroud Channel

A similar procedure have been followed for making the vane seated in the shroud. The vane seat is 3 mm from the shroud bottom inner wall and 4 mm thick. Apart from providing seating for the vane, it also enables uniform flow distribution from the inlet pipe to the channel. The fluid enters the hub channel as a jet exiting from the inlet pipe, impinges on the seat, transforms to uniform channel flow then flows through the vane channel and the hub channel. To have a baseline material for 3D printing four extruded supports are provided in each corners. This is needed as the

3D printing is performed in an inclined angle of 30 degrees from the leading edge position.

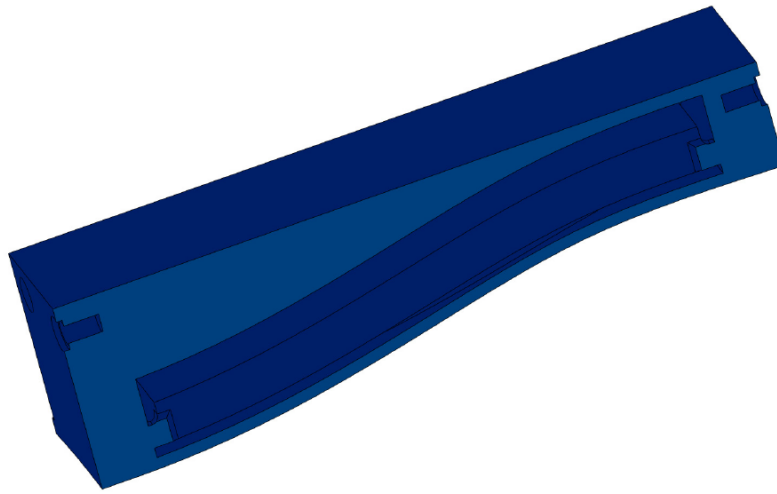


Figure 3.19: Shroud cut section view

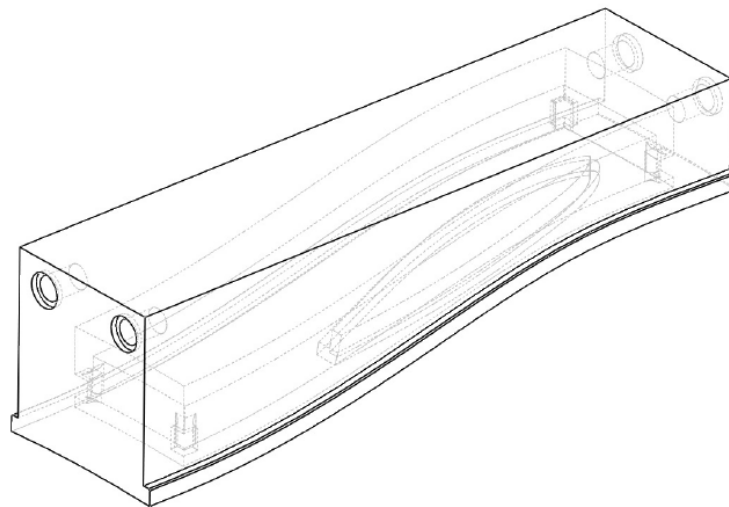


Figure 3.20: Shroud

3.3.4.4 Assembly

In the assembly, hub, shroud and the vane parts have been imported and are automatically placed at the right locations all the parts have been designed based on the common reference planes and axis. Join feature is used for making the assembly. Then, the return channel for the hot water is made from the hub to shroud that return channel exits in the shroud through an outlet pipe. The inlet pipe is also made at the centre of the shroud top face and both these pipes are of same diameter. Fillet is provided for the pipes internally and externally at the shroud top wall to have an additional support. All the chamfers and holes have been made according

to the data from technical drawings. The assembled model is shown in figure 3.21 & figure 3.22. This model is manufactured by rapid prototyping and shown in the figure 3.23.

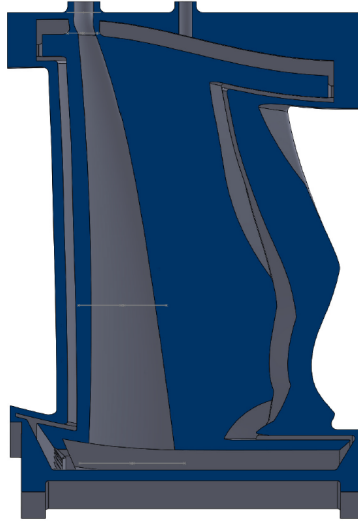


Figure 3.21: Assembled model cut section view

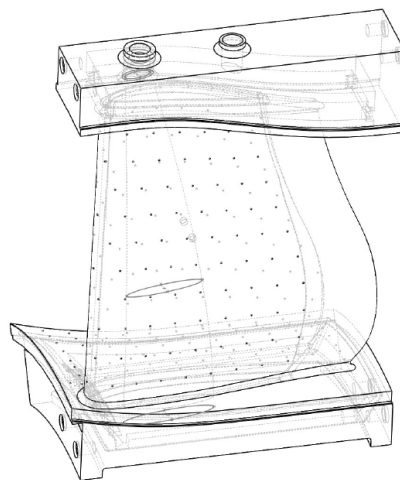


Figure 3.22: Assembly

4

Experimental Methodology

4.1 Experimentation

4.1.1 Rapid Prototyping of the OGV

The designed CAD model is sent to PROTOTAL AB for rapid prototyping by using Stereo Lithography Apparatus (SLA). Accura ClearVue was the material chosen for rapid prototyping. This material has superior properties in terms of heat deflection temperature, which is an important parameter in the present study as the maximum temperature value will be around 50°C. Also, in order to find the material thermal transport properties like thermal conductivity, thermal diffusivity & volumetric heat capacity, two different configurations of the material sample were sent to Hot Disk AB and the corresponding values are tabulated below.

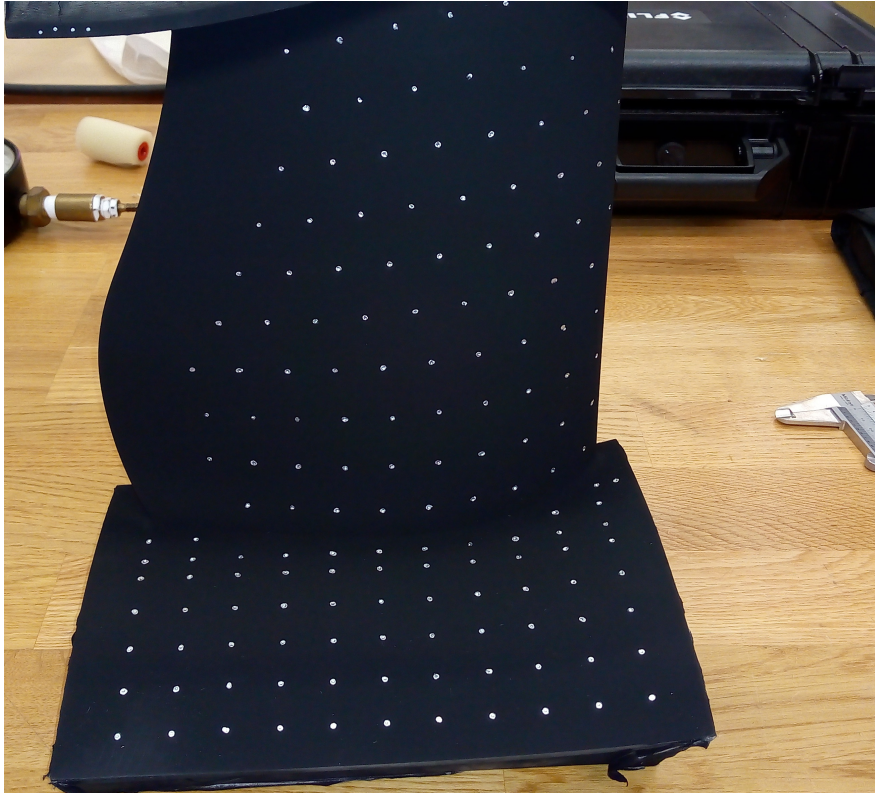


Figure 4.1: OGV Coated with NVC

Table 4.1: Accura Clearvue material properties

Tensile strength	46-53 MPa
Young's Modulus	2270-2640 MPa
Coefficient of Thermal expansion	70
Thermal conductivity	0.220 W/mK
Volumetric heat capacity	1.542 MJ/m ³ K

4.1.2 IR Camera System Calibration

4.1.2.1 Background

In Infrared Thermography, the radiation emitted from the object as photons of interest governed by Planck's law is detected by the IR camera lens. The optical image is then converted into an electronic signals by a thermal sensor known as focal-plane array (FPA) detector elements, which partly absorbs and transmits the photons. The absorbed photons are converted to photo-electrons and are processed by the signal processing unit that converts it to a thermal image.

Thermal radiation is emitted by any object greater than absolute zero temperature and are transported by electromagnetic waves. This mode of heat transfer doesn't require any medium for its transport. In principle, spectral intensity quantification is significant in the evaluation of net radiative flux. For a blackbody, the spectral intensity for a blackbody is given by Planck's law stated below.

$$E_{\lambda,b}(\lambda, T) = \pi I_{\lambda,b}(\lambda, T) = \frac{C_1}{\lambda^5 [\exp(C_2/\lambda T) - 1]} \quad (4.1)$$

where

$E_{\lambda,b}$ - Spectral emissive power

$I_{\lambda,b}$ - Spectral intensity of blackbody radiation

λ - Wavelength

b - blackbody

T - Temperature

C_1 & C_2 - Radiation constants

4.1.2.2 IR Camera

A MWIR Phoenix Camera from FLIR Systems Inc. is used in the present study for thermography measurements. The system consists of a camera head (front end) and real time imaging electronics (back end). The RTIE-based Phoenix camera can be run without analog video output at user specified frame rates and window sizes. A narrow and wide angle lens have been used for capturing the images at two different locations. The specifications of the camera system are tabulated below.

4.1.2.3 Calibrator

A new calibrator is designed for calibrating the IR camera. It consists of a heated aluminum plate embedded with three highly accurate RTD sensors and a differential

Table 4.2: MWIR Phoenix Camera System Specifications

Manufacturer	FLIR Systems Inc.
Model	Phoenix MWIR Camera System
Detector type	Indium Antimonide
Detector spectral Response	$1\mu m - 5.4\mu m$
Filtered spectral response	$3\mu m - 5\mu m$
Format (pixel number)	320 x 256
Detector Pitch	30
Detector Temperature	Stirling cycle
Dynamic Response	77 K
Dynamic Range	14 bit
NETD (sensitivity)	25 mK
Minimum Window	2 rows x 4 columns
Integration mode	Snapshot
Max frame rate full window	122 Hz
Max frame rate minimum window	13.6 kHz
Integration time	$9\ \mu s - 16\ ms$
Output	Composite video/digital image/ RS.232 camera control
Input	Sync (arm/trigger) / RS 232 camera control
Optics	25 mm f/2.3 MWIR / Janos Technology

thermocouple, that gives temperature difference between two locations in the plate. The whole setup enclosed inside a thermocol (Polystyrene) The bottom surface of the hot plate that is painted black with Nextel Velvet Coating (NVC) is viewed by the IR camera. It is designed in such a way that most of the background radiation effects are eliminated by has double isolation. The schematic CAD of the calibrator is shown in the figure.

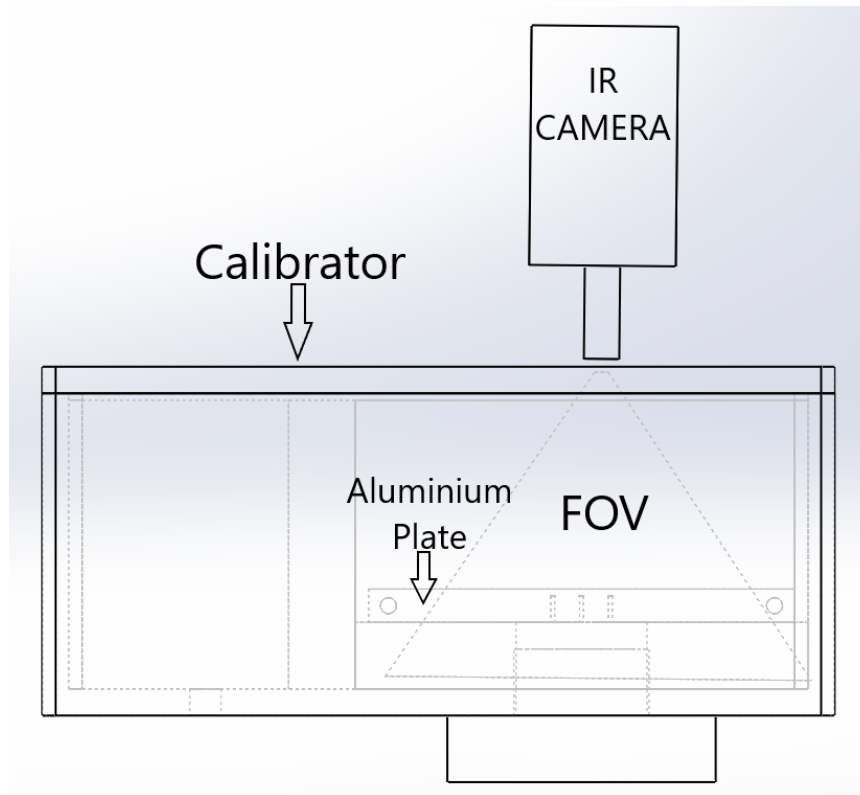


Figure 4.2: Calibration System Design

4.1.2.4 Bad Pixel Association & NUC

After mounting the calibration system and connecting it to a digital computer, the integration time is specified as a first step using the Phoenix camera control software. The selected integration time value of 2.2 ms provides a maximum count value of 12200 at the desired hot temperature value which is around 75% of the FLIR camera dynamic range as per the manufacturer's recommendation. The LabVIEW file which contains the camera calibration interface is started. Before starting with the calibration process, the bad pixel association (BPA) and the non-uniformity correction (NUC) are carried out. Bad or defective pixels are defined as the pixels those being significantly deviating from the average behaviour of their neighbours, arising due to camera manufacturing defects. For this a script is written using MATLAB, that eliminates the bad pixels are associated using special interpolation functions. Since the FLIR camera that uses the focal-plane array (FPA), are generally subjected to non-uniformity of the individual detector array, resulting in spatial variation of the gain and offset parameters known as fixed pattern noise (FPN). Therefore, the

image obtained is degraded and has to be corrected which is termed as the non-uniformity correction (NUC) that calculates the gain and offset coefficients. The two point correction (TPC) based NUC algorithm proposed by [] is used in the present study. The TPC based NUC algorithm is stated as follows

$$y_i(\phi) = [x_i(\phi) - x_i(\phi_1)]g_i + x(\phi_1) \quad (4.2)$$

$$g_i = \frac{x(\phi_2) - x(\phi_1)}{x_i(\phi_2) - x_i(\phi_1)} \quad (4.3)$$

$$o_i = x(\phi_1) - x_i(\phi_1).g_i \quad (4.4)$$

where $y_i(\phi)$ & $x_i(\phi)$ - uncorrected and corrected pixel responses of i th pixel
 $x_i(\phi_1)$ & $x_i(\phi_2)$ - temporal averaged array responses

$x(\phi_1)$ & $x(\phi_2)$ - spatial averaged array responses

g_i & o_i - Gain and Offset coefficients

The images below presents the BPA and NUC process applied to a raw image data.

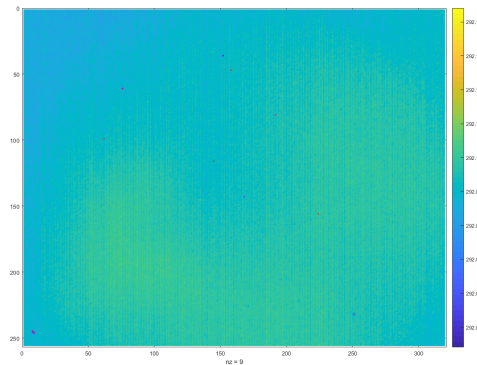


Figure 4.3: Frame with Bad Pixels

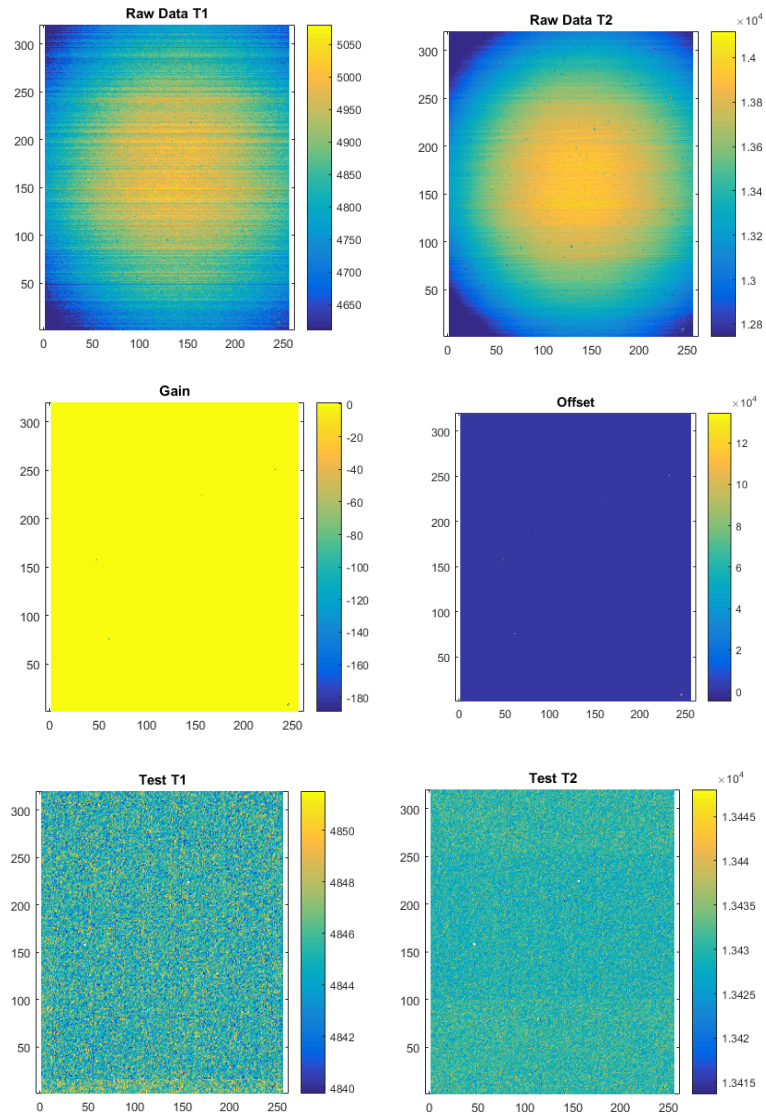


Figure 4.4: Raw image with NUC applied

4.1.2.5 Calibration Process

The Calibration setup is shown in the figure. The camera is made to look upwards to reduce to natural convection effects. A multi-point calibration procedure is followed in the present study for both the narrow and wide angle lenses. The calibrator surface viewed by the camera is nearly considered as a black body with emissivity value around 0.97. Temperature is used as the calibration quantity. The reference Pt100 RTD sensors used for calibration of the camera has an accuracy of $\pm 0.015^\circ\text{C}$. For each temperature points, 100 samples are acquired and stored as a raw data file in matrix format. MATLAB is used to process these files and as a first step these files are temporally averaged to reduce the temporal noise. Later these temporal averaged data are spatially averaged to convert it into a single point value. Then these values which generally represents the camera counts are plotted against the corresponding temperature values read by the RTDs.

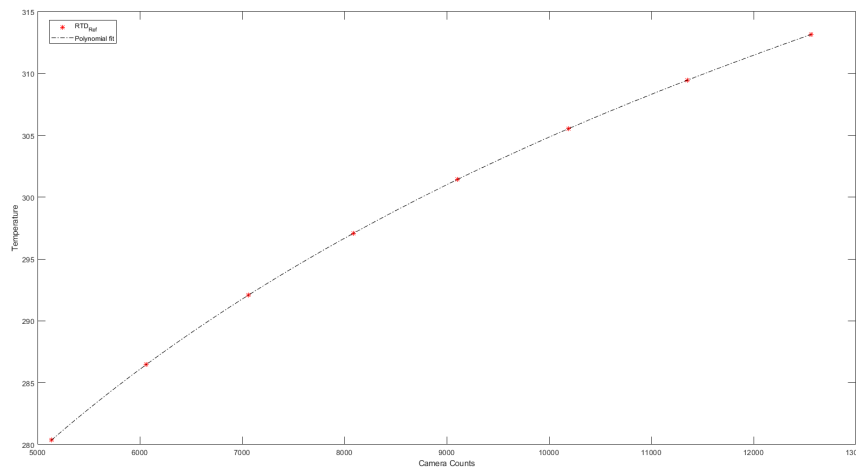


Figure 4.5: Calibration of wide angled lens

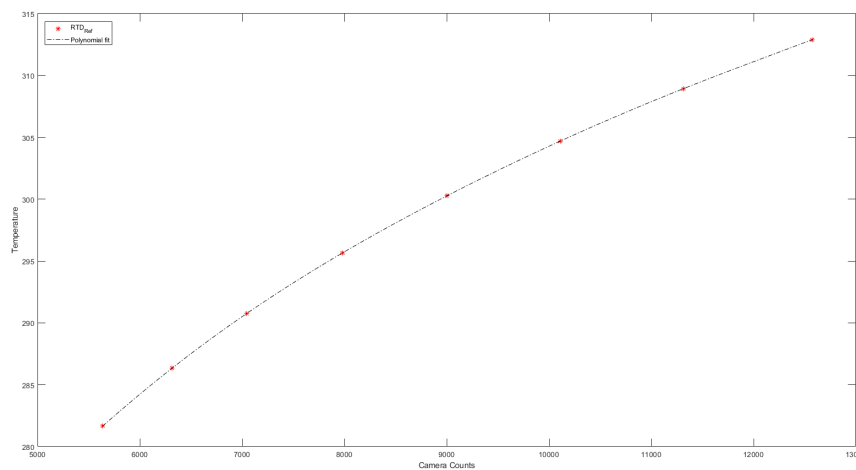


Figure 4.6: Calibration of narrow angled lens

4.1.3 Hot water circulation system

To circulate hot water with a constant mass flow rate, a water circulation system is made. The system consists of a storage tank for water, a pump that circulates water, heating element, and secondary systems like flow regulating valves, pressure gauge, flow meter.

Initially the storage tank is filled with water to a certain level and is heated by a copper coil with water circulation inside. The tank has an excellent insulation with the thermocol layer covering it, preventing heat dissipation to a maximum extent. The hot water is circulated to the vane using a low pressure pump. There is a pressure gauge installed in the direction of inlet pipe to the vane and a flow meter downstream it. The maximum pressure that the pump can provide was measured to be 50000 Pa. On considering the OGV safety limits, the pump is operated at

4. Experimental Methodology

10000 Pa. The maximum mass flow rate recorded by the flow meter is around 0.3 kg/s. A drain valve is provided such that the water flow to the OGV could be stopped and returned to the tank for safety reasons. An RTD sensor is inserted in the water tank that monitors the temperature rise. Before mounting in the TRF, the OGV is tested with the circulation system to ensure fail safe operation. The figure shows the schematic of the circulation system and testing the vane with it. Initially when the vane is tested with water at 45°C, the vane is deformed heavily on the pressure side and the hub region. Therefore a new vane with improved design having a wider return pipe, additional support structures and outlet pipe such that it is invulnerable to failure by deformation.

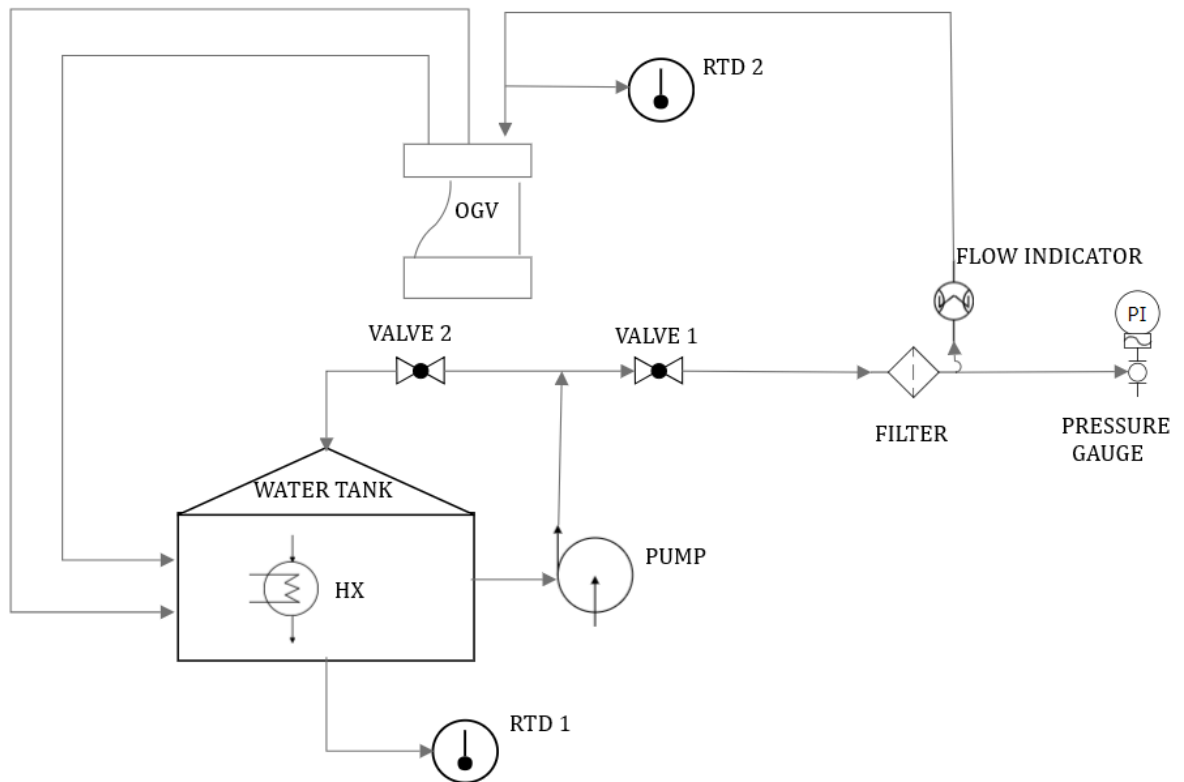


Figure 4.7: Circulation System Schematic

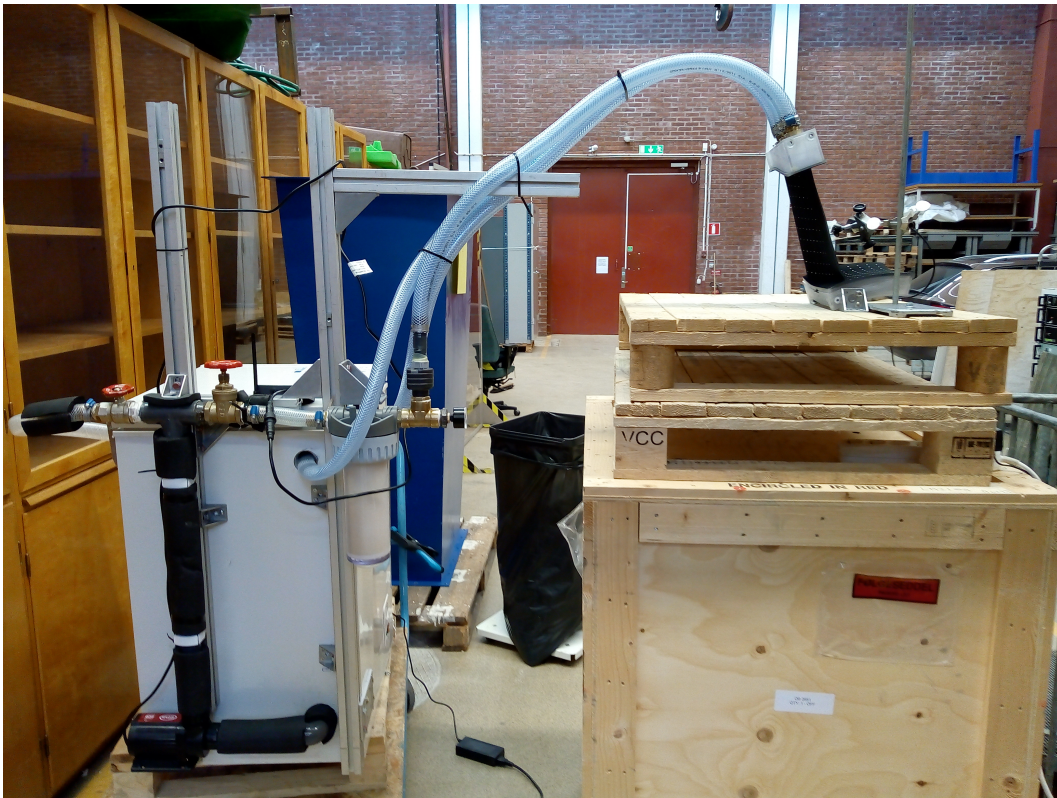


Figure 4.8: OGV with Hot water circulation

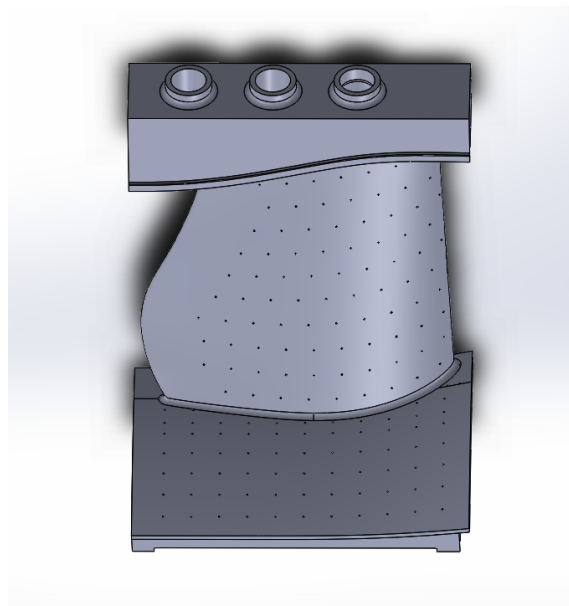


Figure 4.9: Improved CAD Model

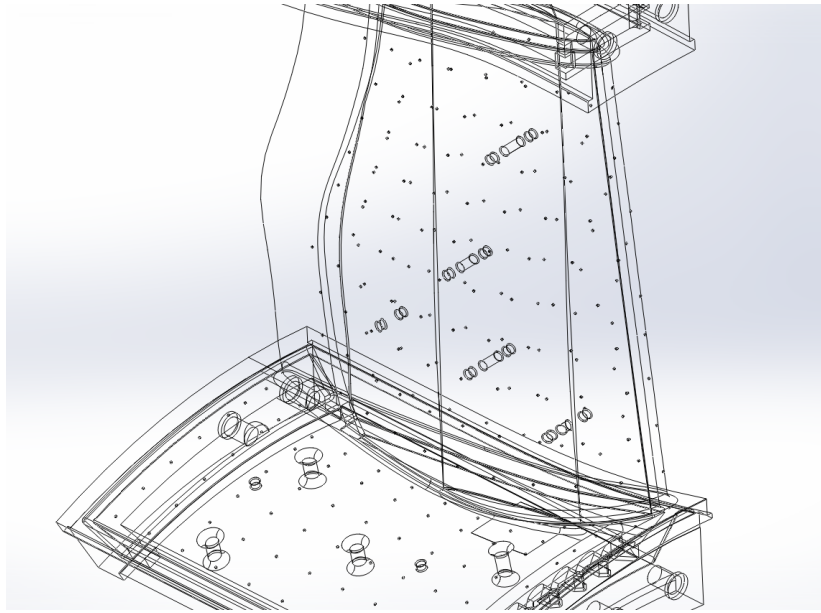


Figure 4.10: Additional Support Structures

Also, the hot water temperature is reduced to 37°C to keep lower amounts of thermal loads and is again connected to the circulation system for testing. When measured with a digital dial gauge, the maximum deformation of the vane at the operating temperature of 37°C , is found to be 0.3 mm which is within the acceptable range. The figure shows the CAD of the newly designed vane. The new OGV is painted with NVC and the markers are made distinct with silver paint. The figure shows the newly designed OGV with NVC.

4.1.4 Preliminary Wind Tunnel test

To get an idea of the desired results and to visualize the temperature distribution on the OGV during the operation of the annular cascade tunnel, a wind tunnel test is made with the IR camera capturing the OGV suction side. A mount for the OGV using FlexLink aluminum profiles such that it extends into the tunnel. The test is carried out at the Chalmers Wind Tunnel. The air velocity is swept from 0 to 15 m/s.



Figure 4.11: Preliminary Wind Tunnel Test

4.1.5 The Experimental Test Rig

The annular cascade tunnel is a semi-closed loop facility rig consisting of a driving section, diffusing section, heat exchanger section, settling chamber, contraction area and the turbine section and finally the TRS test section. The schematic of the annular cascade tunnel rig is shown in the figure and the functionalities of the components are described briefly in the following subsections. For a detailed description, the reader is advised to refer[19].

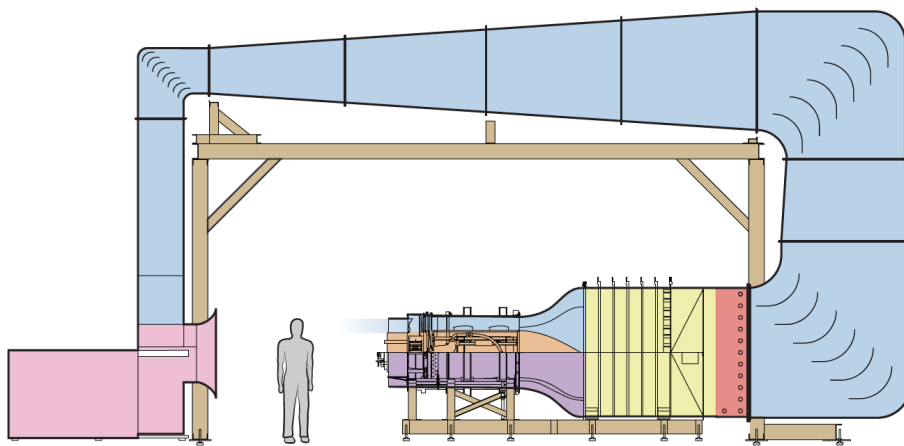


Figure 4.12: Chalmers EEC Test Rig Schematic

4.1.5.1 Driving Fan

The driving fan is located to the left in the figure shown above and is of centrifugal type that provides higher pressure drop and required mass flow to run the turbine. The mass flow could be regulated by frequency converter. The engineering specifications of the fan are tabulated below.

Table 4.3: Wind Tunnel Specifications

Design Volumetric flow rate	6900 m^3/h
Design Total Pressure	7.56 kPa
Fan Diameter	1620 mm
Maximum speed	1800 rpm
Electric motor maximum power	200 kW
Total efficiency	0.82
Noise levels	114.1 dB

4.1.5.2 Diffusing section

The pressure is recovered using the diffuser section. The static pressure of the air that comes from the centrifugal blower increases and enters the larger cross section area upstream of the heat exchanger section. Guide vanes are present in the corners of the duct that not only straightens but also gives a more uniform flow. The diffuser ducts have the half diffuser angle of 3.75° .

4.1.5.3 Heat Exchanger section

The flow then enters the heat exchanger section where it is cooled to 18°C approximately so that the incoming flow to the OGV will be cold. It has a square cross section $2\text{m}\times 2\text{m}$ and water as a working fluid.

4.1.5.4 Settling Chamber

The non-uniformities in the flow that exits from the heat exchanger section are controlled by having a settling chamber downstream. The settling chamber that has the honeycomb and five turbulence screens, conditions the flow and reduces its turbulence intensity.

4.1.5.5 Contraction section

The outlet of the settling chamber is connected to the turbine section via a contraction section, that serves as a location for the mainstream flow rate measurement. It has a length of 1m and an area ratio of 4.7. Apart from improving the flow uniformity, it also increases the velocity downstream.

4.1.5.6 Turbine section

It consists of a braking system and the turbine stage. The braking system is of hydraulic type which is connected to the rotor disk to generate torque required for its speed control. To generate a realistic boundary conditions to the TRS inlet, a turbine stage is located upstream of it shown in the figure. There are 60 NGV and 72 rotor blades in this stage and the latter is shrouded with tip seal to obtain realistic conditions at the OGV inlet.

4.1.5.7 TRS section

Finally the flow enters the TRS section which contains the OGV, which are twelve in numbers. Therefore each OGV sector makes an angle of 30° (five NGVs and six rotor blades for each OGV). There are two traversing systems (one upstream and one downstream of the OGV in the hub) enabling 360° measurements at the respective locations where the former one can traverse just radially while the latter one being able to traverse both radially and axially.

4.1.6 Uncertainty Quantification

The method for uncertainty analysis in the present study is based on the one followed by Osso^[1]. The heat transfer coefficient on the OGV is calculated by the equation 4.5 below which has 7 independent variables assumed to be following a normal distribution.

$$h = \frac{k/t(T_{H_2O} - T_{wall})}{T_{wall} - T_{air}} - \frac{\sigma(\varepsilon_{wall}T_{wall}^4 - \varepsilon_{amb}T_{air}^4)}{T_{wall} - T_{air}} \quad (4.5)$$

The uncertainty can be calculated by the formula

$$\varepsilon_h = \left[\left(\frac{\delta h}{\delta k} \varepsilon_k \right)^2 + \left(\frac{\delta h}{\delta t} \varepsilon_t \right)^2 + \left(\frac{\delta h}{\delta T_{H_2O}} \varepsilon_{T_{H_2O}} \right)^2 + \left(\frac{\delta h}{\delta T_{wall}} \varepsilon_{T_{wall}} \right)^2 + \left(\frac{\delta h}{\delta T_{gas}} \varepsilon_{T_{gas}} \right)^2 + \left(\frac{\delta h}{\delta h_r} \varepsilon_{h_r} \right)^2 \right] \quad (4.6)$$

4.1.6.1 Uncertainty in k

The samples of Accura Clearvue were sent to Hot Disk AB for measuring its thermal conductivity (k) which was found to be 0.22 W/mK and the standard deviation was found to be 0.14%. This is the random uncertainty in k.

4.1.6.2 Uncertainty in t

The OGV wall thickness uniformity is checked by an Ultrasound measurement device which had standard deviations of 0.0534% in the hub surface and 0.0181% on the OGV SS. Therefore the overall uncertainty in thickness (t) is estimated to be 0.068%.

4.1.6.3 Uncertainty in T_{H_2O}

For measuring the water temperature inside the vane channel, a well calibrated Pt100 RTD was used. The mean temperature variations were around 0.011°C . Therefore the uncertainty in T_{H_2O} is estimated to be 0.865%.

4.1.6.4 Uncertainty in T_{wall}

After calibration of the IR camera with the highly accurate RTDs, the difference in the temperature is found to be 0.1°C .

4.1.6.5 Uncertainty in ε_r

The NVC coating has a constant emissivity up to 30 degrees which then drops slowly after 60 degrees to 1%. However this becomes a bias error and is not included in our calculations.

5

Computational Methodology

This section represents the computational modelling of the heat transfer in the OGV. The details regarding the physical configurations, boundary conditions, solving methodology, parameter variation considered and procedure followed for the grid Independence are presented in this chapter.

5.1 Pre-processing

5.1.1 Physical Configurations & Grid Generation

A 3D sector of the OGV model with the hub and shroud is modelled for the CFD simulations. Two computational grids that models the adiabatic and conjugate domains of the OGV are created using the commercial ANSYS ICEM CFD grid generation software. The former contains the grid for the fluid domain only while the latter contains the grid for both fluid and solid domains. The main purpose of testing these two conditions is to find the necessity of solving a conjugate problem and assess the reliability of the adiabatic case against the experiments. A multi-blocking technique is used to create the background three-dimensional mesh for the fluid domain. A fine boundary layer mesh is used near the wall regions to model the flow and heat transfer phenomena to a greater accuracy. The computational domain is simplified by removing the fillet radius of the vane near the endwalls and thickness of the vane for this adiabatic case. A structured hexahedral mesh is generated for the OGV with endwalls sector with a O-grid refinement layer for the vane. The first cell size is chosen based on the desired y^+ value based on a trial and error procedure. On account of the limitations of the computational cost and time, the y^+ value is chosen around 5 and the corresponding first cell size is given near the wall regions. Also further refinement of the first cell size increases the skewness near the trailing edge as the domain is highly 3D. The final grid size is based on the grid convergence studies which are presented in the following section. For the conjugate model, an unstructured grid is generated for the OGV solid part and merged with the fluid domain. The computational domains and the corresponding are shown in the figures.

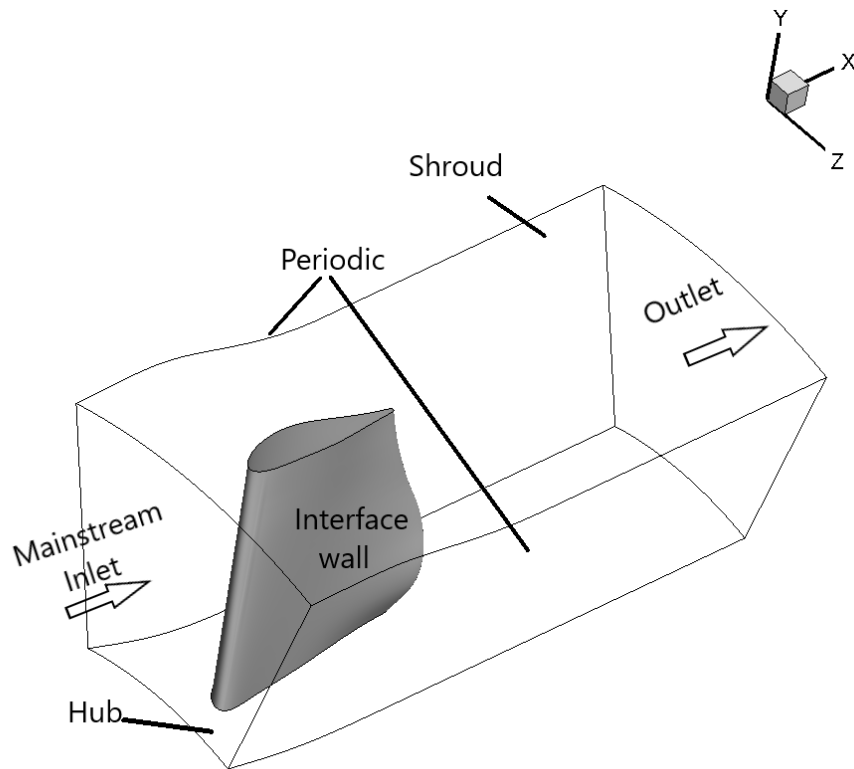


Figure 5.1: Adiabatic Case Domain

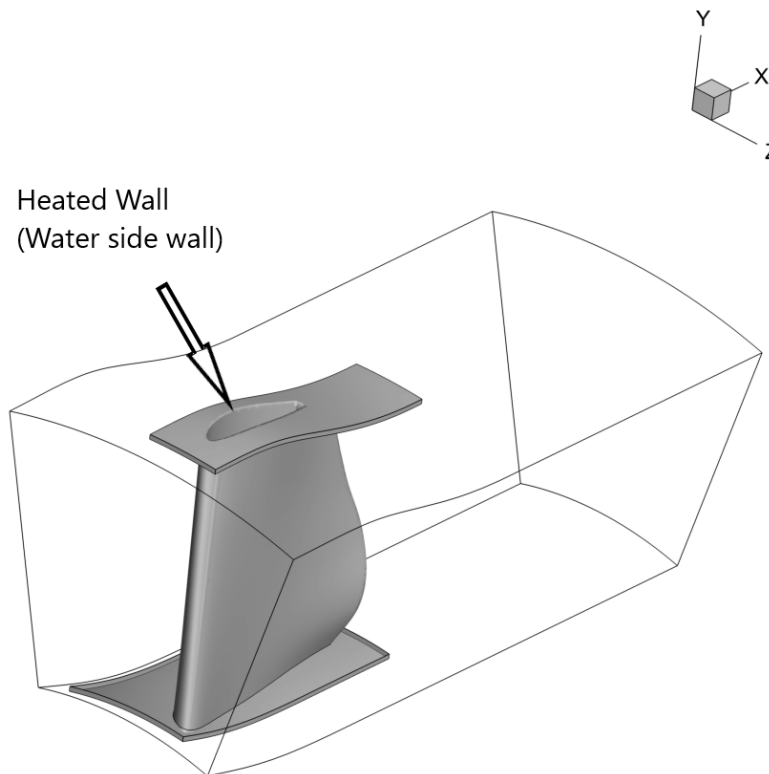


Figure 5.2: Conjugate Case Domain

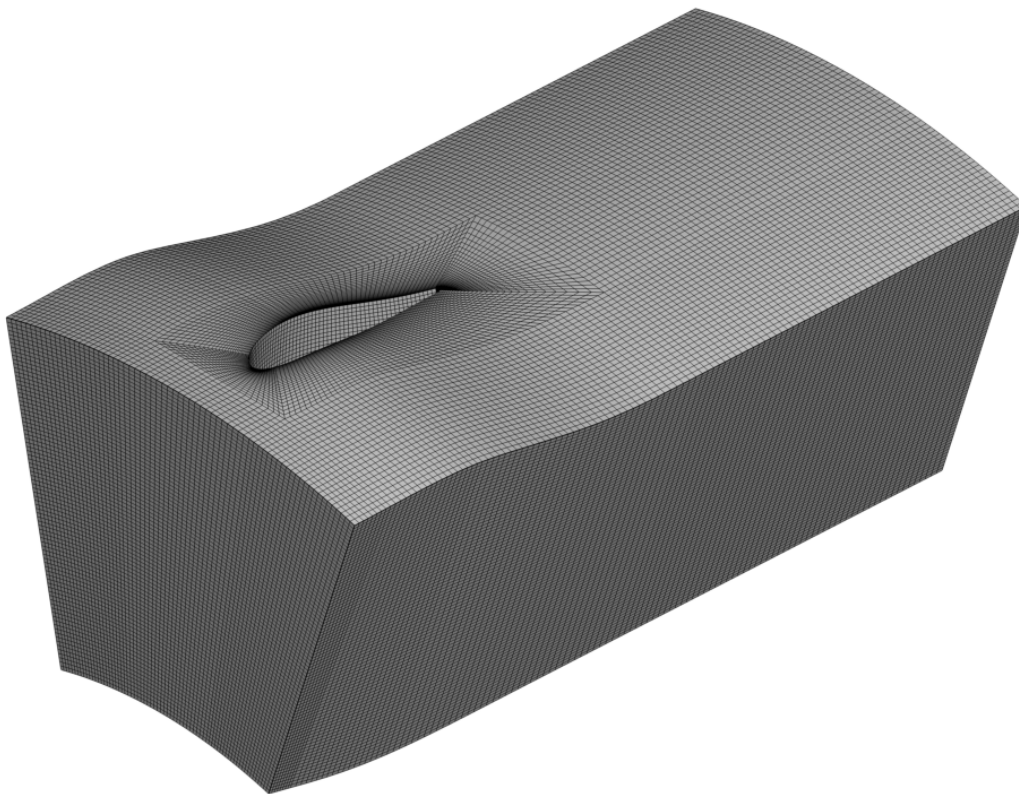


Figure 5.3: Adiabatic Case Mesh

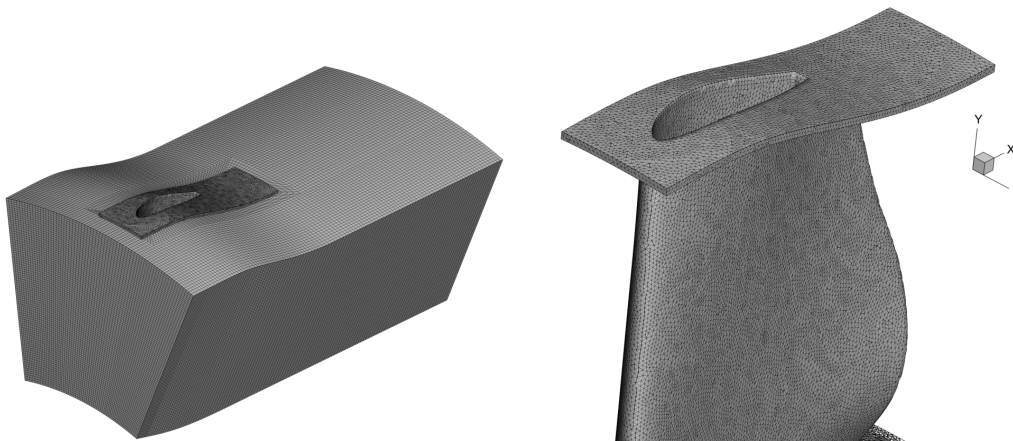


Figure 5.4: Conjugate Case Mesh

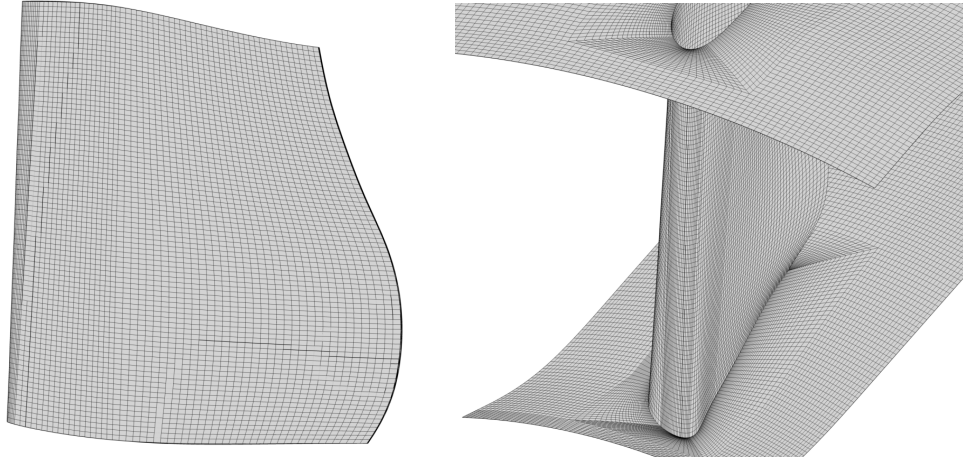


Figure 5.5: Zoomed view of the OGV and End-walls.

5.1.2 Boundary conditions

To simulate the conditions used in the experiments, the values of velocity components in the Cartesian coordinate system from the experimental measurements are specified as a profile inlet condition at the inlet boundary. The temperature at the inlet plane given by the RTD sensor in the experiments is fed as the inlet boundary value in the computations. As the turbulence intensity values in the inlet plane are in the range of 4-6 % from the experiments, a value of 5% is given which is also the typical value in the real-time operating conditions with high turbulent intensity. The turbulent length scale value is based on the channel height which is 0.22 m. Instead of considering a conjugate heat transfer, an adiabatic condition is simulated for simplicity as discussed earlier by eliminating the wall thickness. In order to solve the heat transfer on the OGV wall, a heat flux value is prescribed based on 1D approximations as the vane thickness is mostly uniform. The 1D heat flux approximation is shown as below.

The heat flux q'' is approximated using 1D assumption of the heat conduction from the vane water side to the air side through the wall.

$$q_x'' = k \frac{\partial T}{\partial x} \quad (5.1)$$

$$k \frac{\partial T}{\partial x} = \frac{T_{water} - T_{wall}}{t} \quad (5.2)$$

Assuming

$$T_{wall} = T_{air} \quad (5.3)$$

We know that, $k = 0.22 W m^{-1} K^{-1}$, $T_{air} = 290.84 K$, $T_{water} = 304.68 K$ & Therefore $q_x'' = 761.2 W m^{-2}$

And the side boundaries are defined with rotational periodicity to simulate the annular cascade situation. Typical values for the boundary conditions used are tabulated below.

Table 5.1: Details of the boundary conditions

Boundary Conditions	Values
Mainstream Total Temperature at the inlet, T_{o,∞_i}	290.84 K
Velocity at the inlet plane, $V_{\infty,in}$	Profile inlet
OGV Span, H	0.22 m
Flow Reynolds number, $Re_{\infty,in}$	235000
Flow coefficient, ϕ	0.0622, 0.0588 & 0.0657
Turbulence intensity at inlet and outlet, T.I	5%
Turbulence length scale, T.L	0.22 m
Gauge Static Pressure at the outlet, $P_{s,out}$	-101.053 Pa
Total Temperature at the outlet, $T_{s,out}$	290.84 K
Heat Flux on the OGV, q''	761.2 Wm^{-2}
Water side wall Temperature, $T_{waterside}$	304.68 K

5.2 Grid Convergence study

It is always indispensable for the solution to be insensitive to the spatial grid resolution, a grid convergence study needs to be accomplished. Therefore, a grid convergence study is carried out for the adiabatic case based on the Grid convergence Index (GCI) method [4]. Three levels of grid viz. coarse, medium and fine are used to ensure that the solution lies within the asymptotic range of convergence. The procedure for the GCI method is explained as follows:

To define a representative cell size, the term 'h' is used

$$h = \left[\frac{1}{N} \sum_{i=1}^N (\Delta V_i)^{1/3} \right] \quad (5.4)$$

where, (ΔV_i) is the i^{th} cell volume and N is the total number of cells.

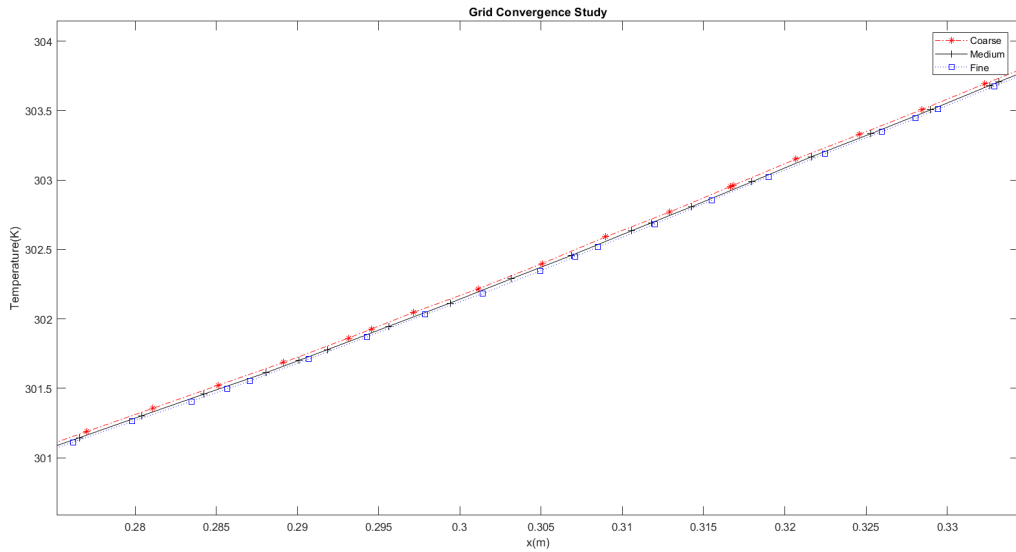
The refinement ratios of each grid refinement levels are defined as;

$$r_{21} = \left[\frac{h_{medium}}{h_{fine}} \right], r_{31} = \left[\frac{h_{coarse}}{h_{fine}} \right], r_{32} = \left[\frac{h_{coarse}}{h_{medium}} \right] \quad (5.5)$$

The values for these grid refinement factors in the present study falls as per the recommendations from the previous researchers that they are greater than 1.1 between two successive grids and greater than or equal to 1.3 for r_{31} . These details of the mesh convergence study are tabulated below. The plot of the grid convergence is shown in the figure where the temperature distribution on the suction side mid-span is plotted against the streamwise distance.

Table 5.2: Details of the Grid Convergence study

Level	N	h	ΔV_i $\times 10^{-8}$	r_{21}	r_{31}	r_{32}
Coarse	855730	0.0030	2.6082	1.1705	1.3825	1.1811
Medium	967555	0.0028	2.288			
Fine	1081932	0.0027	1.9950			

**Figure 5.6:** Grid Convergence study

5.3 Solving Methodology

5.3.1 Governing Equations

The governing equations of the transport process concerning the present study are the equations of mass conservation (continuity equation), momentum conservation and energy conservation are solved along with the RANS based turbulence models.

The following assumptions are assumed while solving the present problem.

- (i) the flow is incompressible
- (ii) the flow is steady
- (iii) the fluid properties are constant
- (iv) the radiation and buoyancy are absent
- (v) viscous dissipation is absent

The governing equations in the differential conservative form can be stated as,

5.3.1.1 Continuity equation

$$\nabla \cdot \vec{v} = 0 \quad (5.6)$$

5.3.1.2 Momentum equation

$$\rho(\vec{v} \cdot \vec{\nabla}) \vec{v} = \vec{\nabla} p + \mu \Delta \vec{v} + \rho \vec{f}_e \quad (5.7)$$

5.3.1.3 Energy equation

$$\nabla \cdot (\vec{v}(\rho E + p) - k \nabla \vec{T} - (\vec{\tau} \cdot \vec{v})) = \vec{f}_e \cdot \vec{v} + q_H \quad (5.8)$$

5.3.2 Turbulence Model

It is of paramount importance to model the turbulence appropriately to validate the computational solution with the experimental data. Based on the operating Reynolds number of 235000, the wall $y+$ value was estimated to be in the range between 5 and 90. Therefore, a RANS based $k - \epsilon$ with standard wall functions and Shear Stress Transport (SST) $k-\omega$ models are used for the closure of turbulence. The plot of the heat transfer coefficient that shows the comparison between these models are shown in figure.

5.3.3 Spatial Discretization Schemes

The governing equations are solved along with the above mentioned standard $k-\epsilon$ and SST $k-\omega$ turbulence models using the finite volume based commercial CFD software FLUENT v18.2. The necessary boundary conditions mentioned in the earlier section are applied to solve the steady state simulations. For the spatial discretization, second order accurate upwind scheme is used for the momentum, energy and turbulent transport equations. A standard interpolation is used for Pressure whereas the SIMPLE algorithm is used for pressure-velocity coupling. To monitor the solution convergence, along with the residual values the area weighted average value of the surface heat transfer coefficient are monitored to reach a steady state values for adiabatic case, while area weighted average value of total surface heat flux on the OGV is monitored for the conjugate case. The steady state is attained when all the residuals are in of order of 10^{-6} for continuity, 10^{-8} for momentum and energy and 10^{-7} for turbulent transport equations.

5.4 Data Representation

For representing the results from the computational solution, it is important to decide the parameters and locations of interest. Since the present computational study is a 3D heat transfer problem, the data are represented by plots & contours of temperature distribution, heat transfer coefficient using lines and planes at the region of interest. The horse-shoe vortex plays a significant role in the flow characteristics at the OGV-hub interface which can be seen from the earlier flow experiments. Therefore for plotting the above mentioned parameters, a curve is extracted on the OGV surface at $0.5H$ (mid-span), where H represents the blade height. The location of the mid-plane curve by lines and planes are shown in the figures 5.7 and 5.8. Tecplot 360 is used for representing the data in contours using flooded line values for better visualization and CFD Post from ANSYS is used for extracting the mid-span curve.

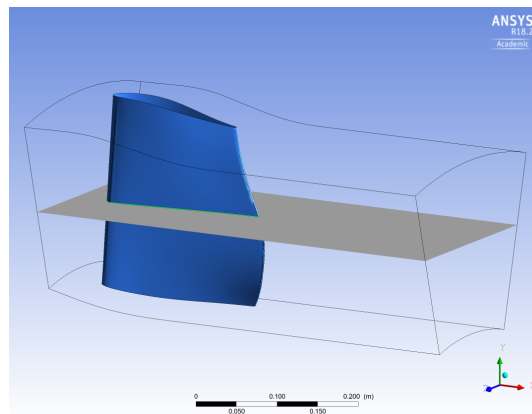


Figure 5.7: Mid-span Plane

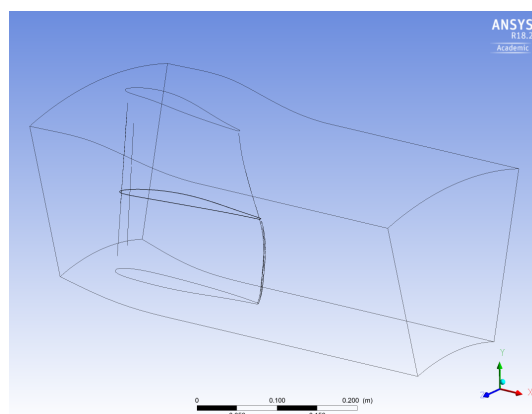


Figure 5.8: Mid-span curve

6

Results & Discussions

This chapter presents the results and discussions concerning the experimental and computational investigations of the heat transfer measurements on the OGV suction side. Contours and plots of Temperature and Heat Flux are used to explain the results for three different flow coefficient values simulating the on-design and off-design conditions for a constant engine operative Reynolds number value of 235000. The three different flow coefficients with their corresponding exit swirl angles and loading coefficients are tabulated below as the test matrix. The flow coefficient (ϕ), is defined as the ratio of the meridional velocity to the blade speed.

$$\phi = c_m/U \quad (6.1)$$

where c_m is the meridional velocity and U is the blade speed.

6.1 Post Processing of the Experimental Results & Estimation of Heat Transfer Coefficient

The calculation of the heat transfer coefficient (HTC) by experiments is the prime objective of this study, since the IR camera gives the temperature data only, an algorithm for calculation of HTC is necessary. The BPA and NUC is applied for the raw data captured by the IR camera by grabbing a decided number of frames specified in the section 4.1.2.5 of chapter 4. The temperature data obtained by the IR camera is in the format of 2D, but to calculate the HTC on the blade surface which is 3D in real-time, for which a 3D temperature distribution is needed. Therefore mapping of the 2D temperature to the 3D temperature on the OGV suction side is necessary. For mapping the vane markers are used. A MATLAB script is used for mapping the marker locations with the OGV 3D data coordinates by manual

Table 6.1: Test matrix

Re	ϕ	α	ψ	Operating Condition
235000	0.622	-16.4	1.153	On Design
	0.588	-31.4	1.274	Off Design (High loading)
	0.657	-11.4	1.035	Off Design (Low loading)

selection of the points. Therefore the 2D temperature profile is now converted to a 3D on the OGV surface. This 3D temperature data on the OGV outer surface (air side) along with the constant temperature on the inner surface (water side) will be used as a boundary condition for solving the heat flux from which the HTC can be calculated. For solving this conduction, the FEATool in MATLAB is used.

6.2 A Brief Review of Secondary Flow Influence on Heat Transfer

The flow impinges on the leading edge of the OGV, called as the stagnation region where it is split into two parts. By the classical secondary flow vortex system described by Sieverding [3], rolling up of the endwall boundary layer results in a vortical motion forming a horseshoe vortex which is generally true for most of the turbomachinery flows. These secondary flow has a greater influence on the heat transfer behaviour as the convective heat transfer is always associated with the flow physics. It can be observed from the previous literature that the suction side of the vane, has got the most significant flow and heat transfer characteristics due to transition in the boundary layer or separation. Therefore, the present study results are discussed based on the suction side results.

6.3 Temperature Distribution

The temperature distribution for the three different flow coefficient values are presented with the contours of temperature from the experiments and CFD, supported by their corresponding plots. It can be seen from the experimental results, that the stagnation zone data is trimmed due to the missing leading edge temperature data. In general this stagnation zone records the lowest temperature values, after which the temperature gradually increases and attains a peak in the mid-chord region and decreases again. This transition phenomena is not very well predicted by the adiabatic CFD calculations. However, the conjugate CFD calculations predicts this behaviour comparatively better with an offset. The horseshoe vortex formation can be seen near the hub and OGV interaction area, where there is an increase in the temperature value observed. Therefore, to visualize this phenomena, a plot comparison of Temperature is made on the mid-span curve on the suction side for all the cases which actually supports the above mentioned discussion.

It can be seen that the experiments that the temperature first increases up to 20% of the streamwise distance, with less steep further up to 60% of the streamwise distance, after which there is a gradual drop and remains almost constant. For the corresponding CHT based CFD results, however a constant trend is seen after 20% of the streamwise distance until 80%. After that there is a gradual decrease till the end. The overall comparison plot for the experimental temperature distribution data shows that the flow coefficient(ϕ) value of 0.657 has this transition behaviour closer to the leading edge compared to the other two cases.

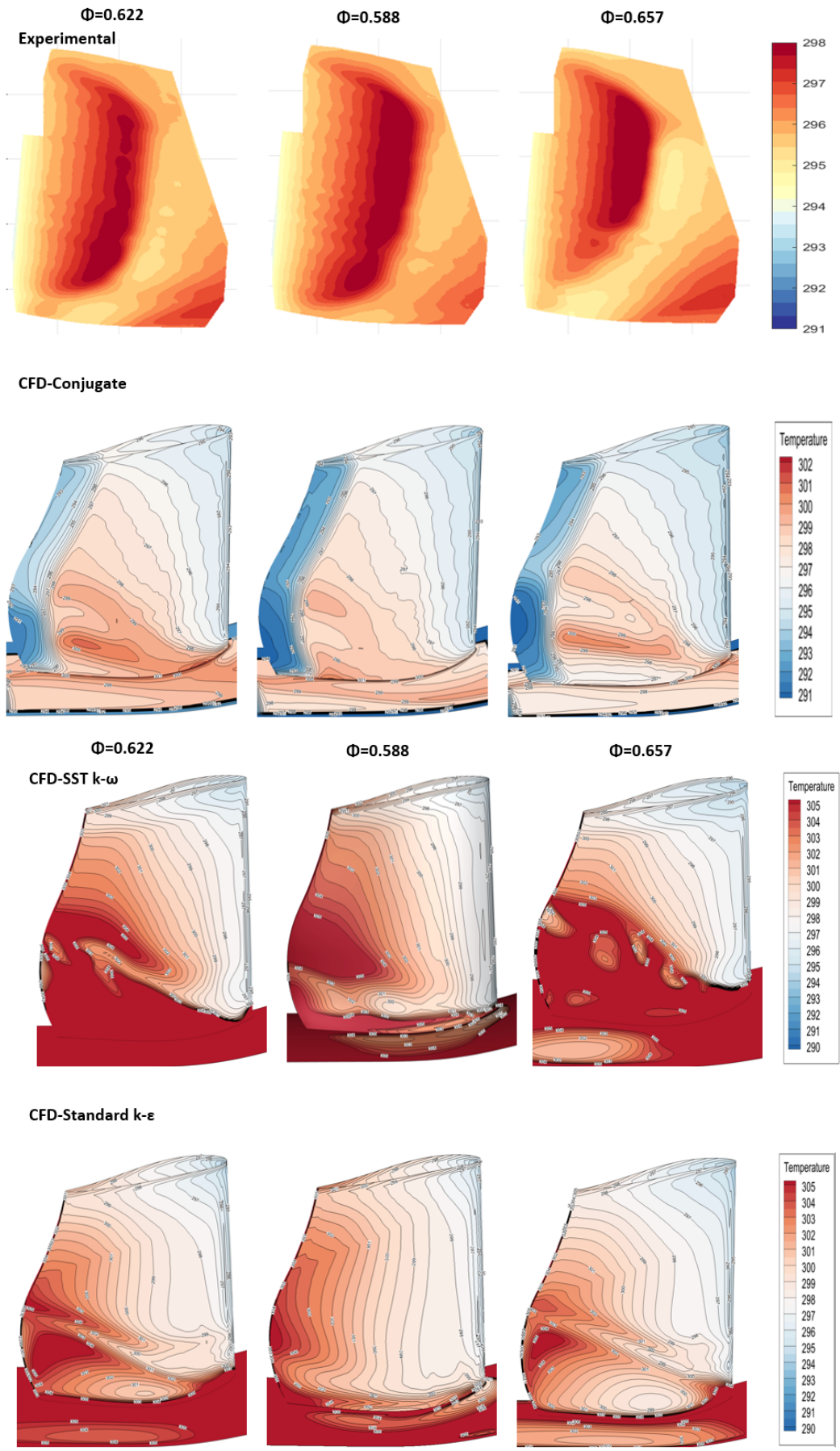


Figure 6.1: Contours of Temperature Distribution

6. Results & Discussions

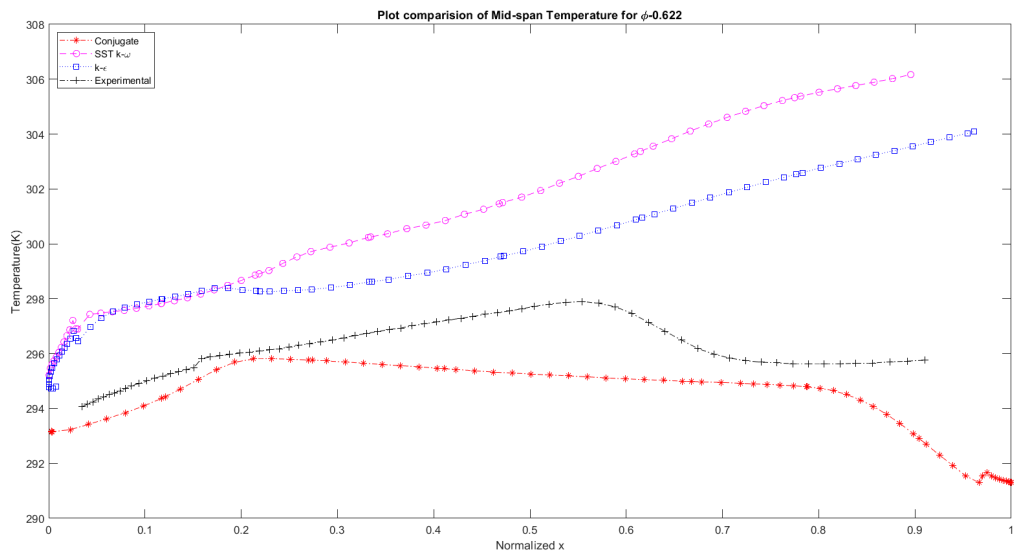


Figure 6.2: $\phi = 0.622$ -Comparison of Mid-span Temperature Distribution

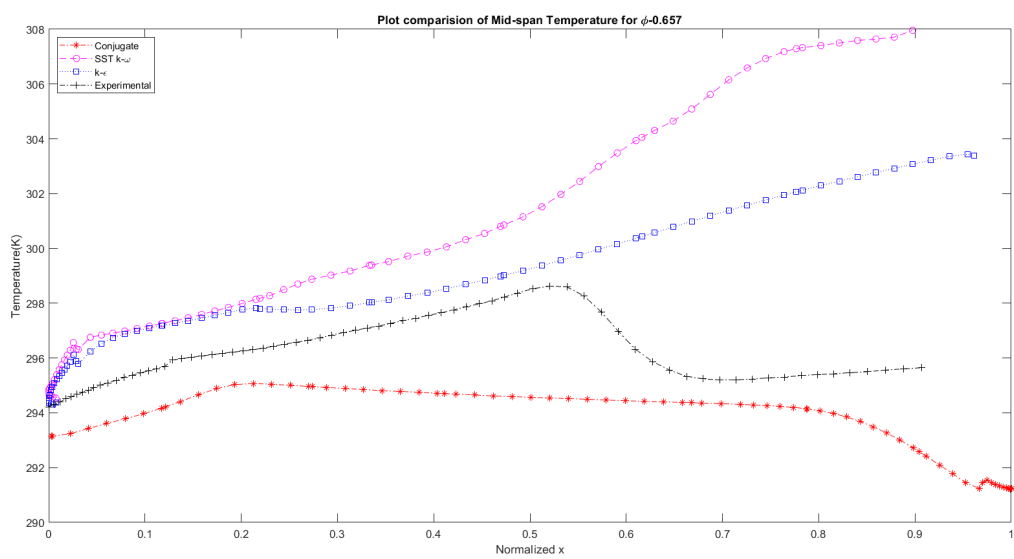


Figure 6.3: $\phi = 0.657$ -Comparison of Mid-span Temperature Distribution

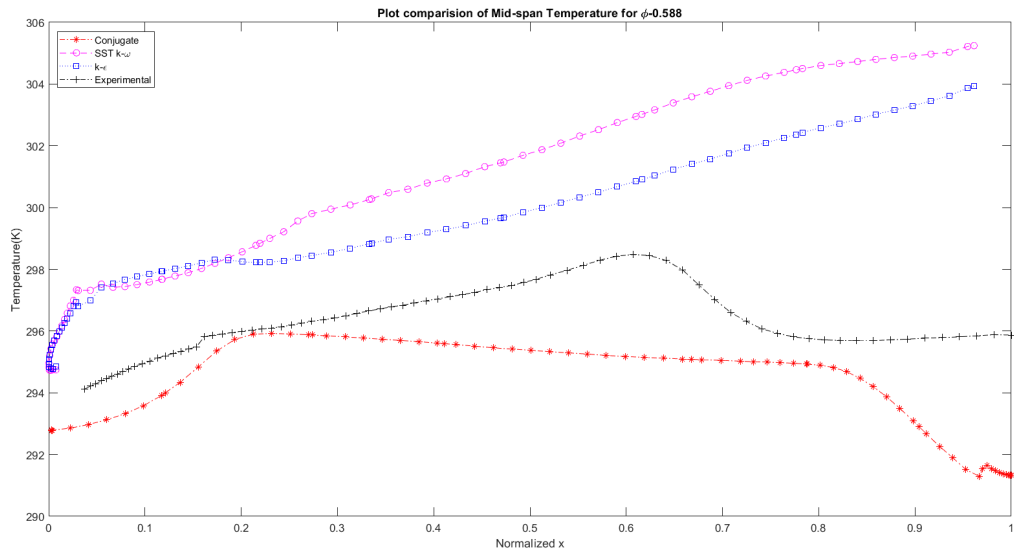


Figure 6.4: $\phi = 0.588$ -Comparison of Mid-span Temperature Distribution

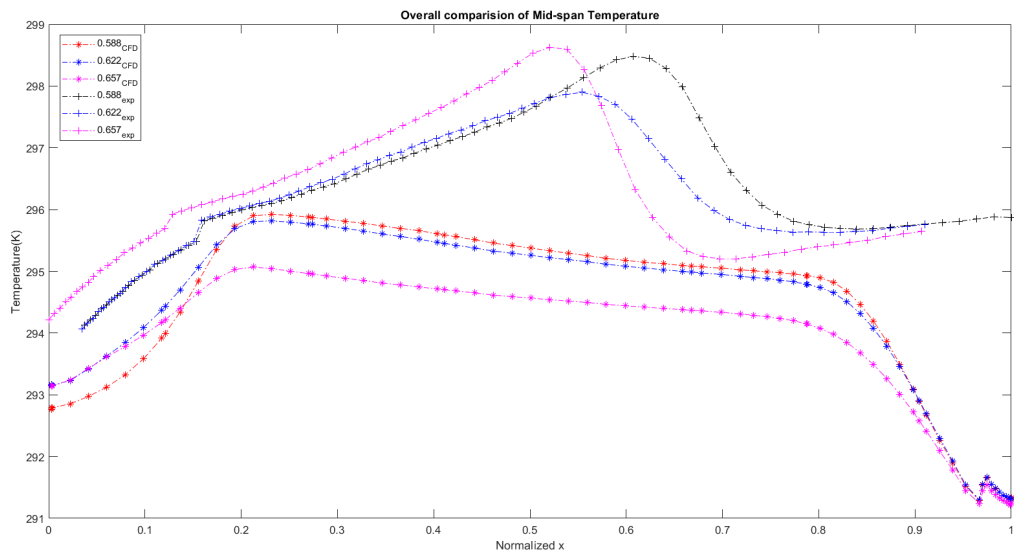


Figure 6.5: Overall Comparison of Experimental & Conjugate CFD Temperature Distribution

6.4 Heat Transfer Coefficient Distribution

It can be seen from the plots of overall heat transfer coefficient (HTC) comparison presented in figure 6.6, that the experimental values are highest near the leading edge and decreases to the lowest value in the mid chord area. It then increases suddenly from that point to the downstream region and becomes the lowest in the trailing edge zone which is not visible here due to missing information. The sudden increase may be because of transition in the boundary layer from laminar to turbulent or due to a laminar separation bubble. Again this sudden transition in the heat transfer is not very well captured by the CFD results which could be inferred from the plots of the conjugate CFD results. In both experimental and CFD results, the flow coefficient(ϕ) value of 0.657 has the highest magnitude of HTC especially after the transitional behaviour. The contours of HTC by experiments and CFD supports this discussion. Also, the CFD results are over-predicted which may be due to poor performance by the RANS based turbulence models for this type of problem.

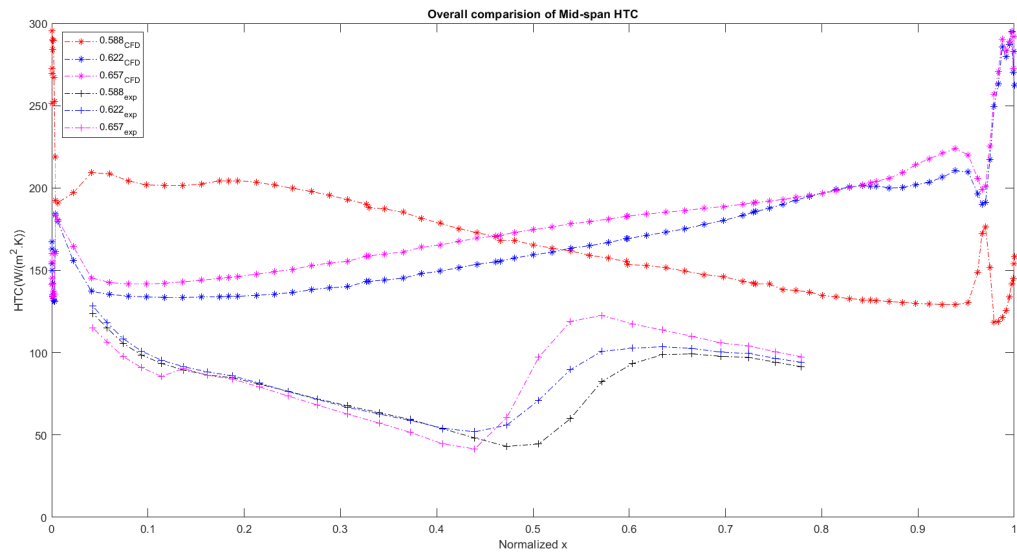


Figure 6.6: Overall Comparison of Experimental & Conjugate CFD HTC Distribution

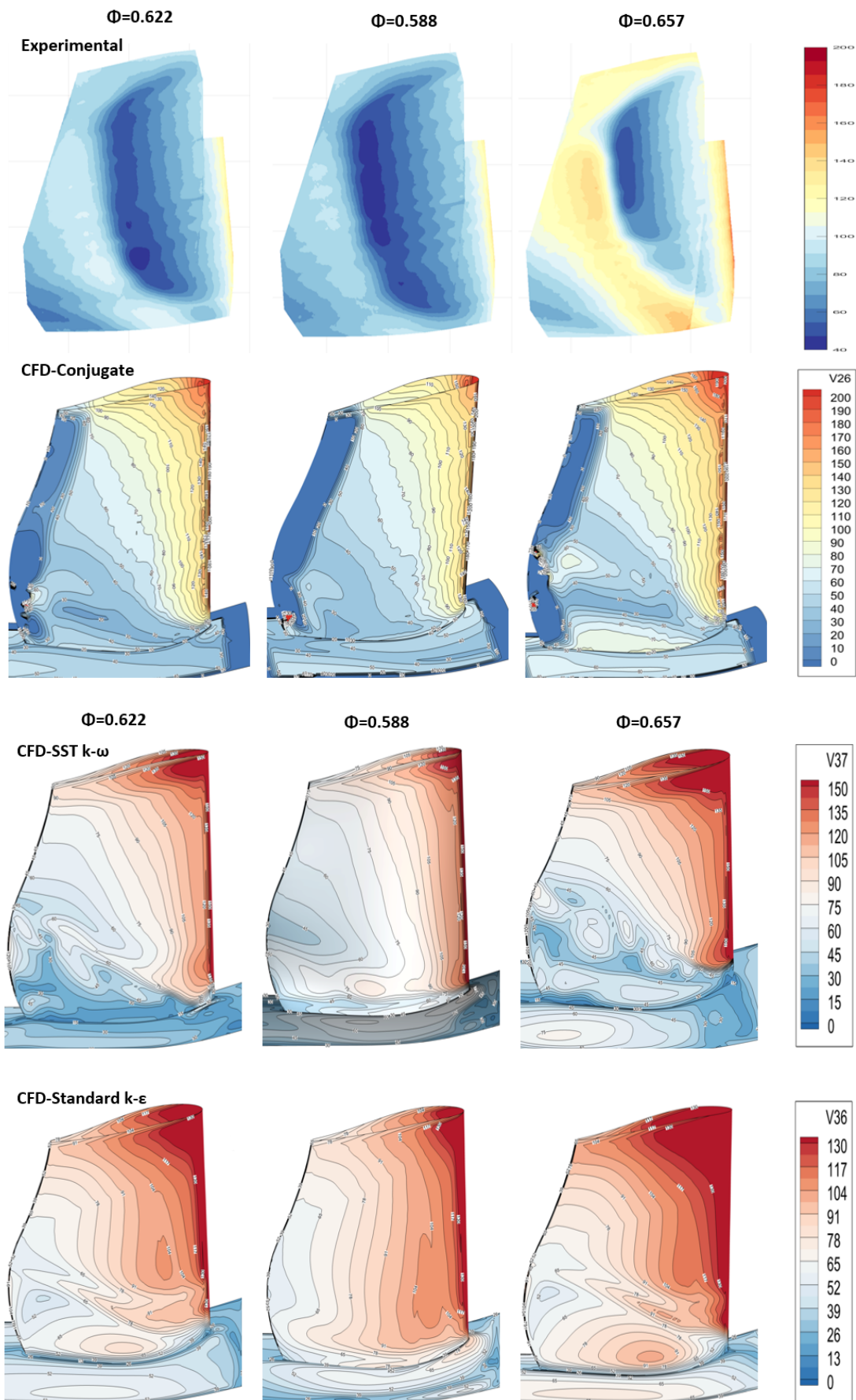


Figure 6.7: Contours of HTC Distribution

7

Conclusion

The prime objective of the thesis is to estimate the heat transfer coefficient on an OGV of the Engine Exit Module (EEM) at the Chalmers turbine facility, by Infrared Thermography experiments along with the commercial code CFD software. The OGV heat transfer model is prepared by Rapid Prototyping technique with a channel for uniform circulation of the hot water. A multi-point calibration procedure has been followed for the IR camera. The experimental measurements and the computational simulations are carried out at the engine representative flow Reynolds number of 235000 for three different flow coefficient values.

The calibration and the measurements resulting from the experiments are highly accurate. A novel heating design is made for the OGV and the endwalls by circulating hot water that provides uniform heat transfer to the maximum surface of the OGV. Computational simulations of the OGV sector are performed by commercial CFD tools. Two different cases (Adiabatic and conjugate) of the OGV have been solved using two different RANS based turbulence models. The adiabatic model solves only the convection heat transfer by enforcing a uniform surface heat flux boundary condition on the heated walls using 1D heat conduction assumptions and the conjugate model solves the convection and conduction associated with the OGV by considering the thickness of the real time experimental model.

The results of the CFD are compared with the measured experimental data and the following inferences about the heat transfer distribution on the suction surface of the OGV have been made.

- The effects of the horse-shoe vortex (HSV) near the OGV and hub endwall interface has been well captured by the experiments and the computations.
- There exists a transition in the heat transfer pattern from the experiments in the mid-chord region of the OGV suction surface which may arise due to a boundary layer transition or a separation bubble, which is not predicted by the adiabatic CFD simulations in all the cases.
- The conjugate heat transfer model predicts this transitional behaviour but with an offset to the farther downstream location and the values are under predicted.

7.1 Scope for Future Work

The present work deals with a low Reynolds number of 235000 which is also an engine representative condition but with limitations to few engine models and without considering the purge flow that emanates from the hub side entrance. Therefore, one could study this purge flow and also with high Reynolds number. The transitions happening in the experimental data could be studied in detail by resolving the boundary layer using hot wire measurements and advanced flow visualization methods like Particle Image Velocimetry (PIV).

Bibliography

- [1] Turner, A. B. (1971) Local Heat Transfer Measurements On A Gas Turbine Blade Cascade, *Journal of Mechanical Engineering Science*, Vol. 13 issue: 1, pp: 1-12
- [2] Graziani, R.A., Blair, M.F., Taylor, J.R., Mayle, R.E. (1980) An Experimental Study of Endwall and Airfoil Surface Heat Transfer in a Large Scale Turbine Blade Cascade, *ASME Journal of Power Engineering*, Vol. 102, pp: 25-357.
- [3] Sieverding, C. H. (1985) Recent Progress in the Understanding of Basic Aspects of Secondary Flows in Turbine Blade Passages, *ASME Journal of Engineering for Gas Turbines and Power*, Vol. 107, pp: 248-257
- [4] Roache P.J. (1994) Perspective: A Method for Uniform Reporting of Grid Refinement Studies. *ASME. J. Fluids Eng.* 1994;116(3):405-413. doi:10.1115/1.2910291
- [5] (2008) Procedure for Estimation and Reporting of Uncertainty Due to Discretization in CFD Applications. *ASME. J. Fluids Eng.* 2008;130(7):078001-078001-4. doi:10.1115/1.2960953
- [6] Arroyo Osso C, *Aerothermal Investigation of an Aggressive Intermediate Turbine Duct*, Doctoral thesis, 2009, Chalmers University of Technology, 978-91-7385-351-4
- [7] Arroyo Osso C, Gunnar Johansson TT, Wallin, F. (2010) Heat Transfer Investigation of an Aggressive Intermediate Turbine Duct: Part 1—Experimental Investigation, *Proceedings of ASME Turbo Expo 2010: Power for Land, Sea and Air*, pp: 605-613
- [8] Wallin F., Arroyo Osso C. (2010) Heat Transfer Investigation Of An Aggressive Intermediate Turbine Duct: Part 2 - Numerical Analysis, *Proceedings of ASME Turbo Expo 2010: Power for Land, Sea and Air*, pp: 81-89
- [9] Marcotte, F., Tremblay P., Farley, V. (2013) Infrared camera NUC and calibration: comparison of advanced methods, *Proceedings of SPIE*, 10.1117/12.2016265
- [10] Arroyo Osso C, Gunnar Johansson TT, Wallin F. *Experimental Heat Transfer Investigation of an Aggressive Intermediate Turbine Duct*. *ASME. J. Turbomach.* 2012;134(5):051026-051026-10. doi:10.1115/1.4004779
- [11] Wang, C., Wang, L., Sunden, B., Chernoray, V., Abrahamsson, H., (2014) An Experimental Study of Heat Transfer on an Outlet Guide Vane, *Proceedings of ASME Turbo Expo 2014: Turbine Technical Conference and Exposition*, Vol. 5B, 10.1115/GT2014-25100

- [12] Merina, C.M. (2015) Experimental heat transfer measurement technique validation and measurements in a linear cascade of an OGV and endwall, Master's Thesis in Solid and Fluid Mechanics, Chalmers University of Technology
- [13] Wang, C. [2015] Experimental and numerical investigation of outlet guide vane and endwall heat transfer with various inlet flow angles, *International Journal of Heat and Mass Transfer*, Vol. 95, pp: 355-367
- [14] Mayo I, Cernat BC, Virgilio M, Pappa A, Arts T. (2016) Aerothermal Investigation on the Flow and Heat Transfer in a Helically Corrugated Cooling Channel. ASME. Turbo Expo: Power for Land, Sea, and Air, Volume 5B: Heat Transfer ():V05BT16A017. doi:10.1115/GT2016-57606
- [15] Orzanowski, T. (2016) Nonuniformity correction algorithm with efficient pixel offset estimation for infrared focal plane arrays, SpringerPlus, 10.1186/s40064-016-3534-1
- [16] Singh, P., Ji, Y., Zhang, M., Ekkad, S. V. (2017) Heat Transfer Enhancement by Criss-Cross Pattern Formed by 45° Angled Rib Turbulators in a Straight Square Duct, Vol. 01, 10.1115/HT2017-4908
- [17] Ornano F, Povey T. (2017) Experimental and Computational Study of the Effect of Momentum-Flux Ratio on High Pressure NGV Endwall Cooling Systems. ASME. Turbo Expo: Power for Land, Sea, and Air, Volume 5C: Heat Transfer ():V05CT19A017. doi:10.1115/GT2017-64229
- [18] Elfner M, Schulz A, Bauer H, Lehmann K. (2017) A Novel Test Rig for Assessing Advanced Rotor Blade Cooling Concepts, Measurement Technique and First Results. ASME. Turbo Expo: Power for Land, Sea, and Air, Volume 5A: Heat Transfer ():V05AT16A015. doi:10.1115/GT2017-64539
- [19] B. Rojo, Aerothermal Experimental Investigation of LPT-OGVs, Doctoral thesis, 2017, Chalmers University of Technology, 978-91-7597-645-7
- [20] Wang, N., Chen, A. F., Zhang, M., Han, J. C. (2018) Turbine Blade Leading Edge Cooling With One Row of Normal or Tangential Impinging Jets, *ASME Journal of Heat Transfer*, Vol. 140